12

Multiscale Models of Flow and Transport

Ilenia Battiato
San Diego State University

12.1 Introduction: A Question of Scale

> Everything should be made as simple as possible but not simpler.
>
> **A. Einstein**

One of the most significant challenges that hydrogeologic modelers continue to face is the "tyranny of scales" [1] in hydrologic systems, that is, the disparity of temporal and spatial scales at which mass, momentum, and energy transport is best understood (e.g., subpore to pore scale and seconds to days) and at which predictions are needed for practical applications (e.g., plume to aquifer scale and years to centuries) (see Figure 12.1). This is typical in remediation strategies of contaminated sites; management of water resources; petroleum, gas, and geothermal energy production; and geological CO_2 sequestration, which require long time predictions over large spatial scales. Achieving a *predictive understanding* of hydrological systems response to anthropogenic stressors and environmental changes, and the associated risks [2], is a primary societal need since long-term strategies to accommodate ever-increasing energy demands, to control atmospheric CO_2, and to understand nutrient cycles need first to be evaluated and then implemented. Modeling approaches that incorporate process understanding at different temporal and spatial scales, here referred to as multiscale models, are therefore necessary to improve our predictive capabilities of natural systems.

While it is recognized that much progress has been made in modeling at-scale systems from the pore to the field scale, the appropriate level of hydrogeologic model complexity has been actively debated in the recent literature [3,4] and continues to pose a challenging problem. In particular,

> fragmentation of science, technologies, and predictive capabilities among disciplines and the focus on studying mostly individual, scale-based system components [···] leads to fundamental uncertainties about how coupled subsystems interact with each other and respond to environmental changes across different space and time scales. The lack of sufficient science-based capabilities to predict these interactions and responses hinders the ability to sustainably manage and mitigate energy and environmental problems [5].

As highlighted in a 2007 Department of Energy report [6], an opportunity for advancement lies in the development of a new generation of "multi-physics capabilities that offer seamless modeling of processes over multiple scales." Yet, the difficulty in linking transport processes *across scales* arises because subsurface flow and transport take place in complex highly hierarchical heterogeneous environments [7–10] and pervasively exhibit

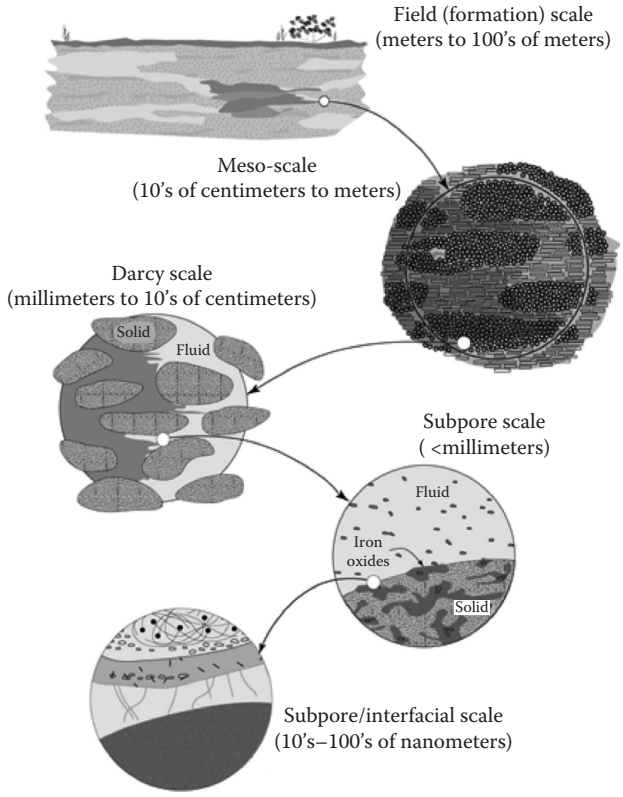

FIGURE 12.1 Hierarchy of scales in subsurface systems. (Adapted from http: //sbi.oregonstate.edu/news/200903.htm.)

nonlinear dynamics and partial or total lack of (temporal and spatial) scale separation, that is, physical and biogeochemical phenomena on one scale (e.g., a pore scale) affect, and are coupled to, phenomena on a vastly different scale (e.g., a field scale). For example, pore-scale molecular diffusion fundamentally affects field-scale mixing of (bio)chemically reacting solutes [11]. Similarly, strong coupling of flow and reactive transport dynamics is critical during CO_2 injection into geologic formations, where the interaction between the fluid and the host rock triggers rock structure modifications that can either improve or impair its permeability [12–16]. Conversely, local pore-structure alterations may largely control the injectivity, the pressure field dynamics, and CO_2 spreading [17]. Other examples include radionuclide transport in the subsurface [18] and biogeochemical processes in the hyporheic corridor that can lead to local modification of the porous matrix and its physicochemical properties [19].

For such inherently multiscale systems, the *development* of physics-based models follows a *bottom-up* approach. Through rigorous upscaling techniques, it is possible to construct effective-medium representations of fine-scale processes with different degrees of coupling and complexity [21]. Yet current *model deployment* is generally based on established engineering practices (and/or experts' personal experience) and often relies on classical continuum descriptions without an *a priori* evaluation of their validity as predictive tools. While the ubiquitous presence of heterogeneities in natural systems might lead to a localized breakdown of continuum (Darcy-scale) models, in many applied disciplines, the transition from theoretical modeling to practical applications poses the danger of losing track of modeling assumptions. Resulting failure can be dramatic in both social and economic terms, with miscalculation of oil recovery rates and contaminant migration [22]. The formulation of rigorous "diagnosis criteria" for the applicability of effective-medium representations can help resolve the apparent chasm between modelers and practitioners by providing information about the scale (e.g., subpore, pore, Darcy, field) at which effective parameters can be most appropriately defined and data collected, while guaranteeing that the coarser scale model is employed, wherever and whenever possible. Such an approach will help bridge the gap between the *develop*ment of rigorous bottom-up multiscale physics-based models and their optimal top-down *deploy*ment in real-world applications where accuracy and computational burden need to be balanced. The proposed linkage between rigorous physics-based model development and deployment is sketched in Figure 12.2. A critical first step toward the development of an integrated multiscale modeling framework that is predictive and optimal is the understanding of the interactions between physical and biogeochemical processes across multiple scales: yet, the accurate coupling of two (or more) models operating on vastly different spatial and/or temporal scales remains a major theoretical and computational challenge.

In this chapter, we review current approaches to incorporate multiscale dynamics into model development and some of the upscaling techniques that can be employed to establish

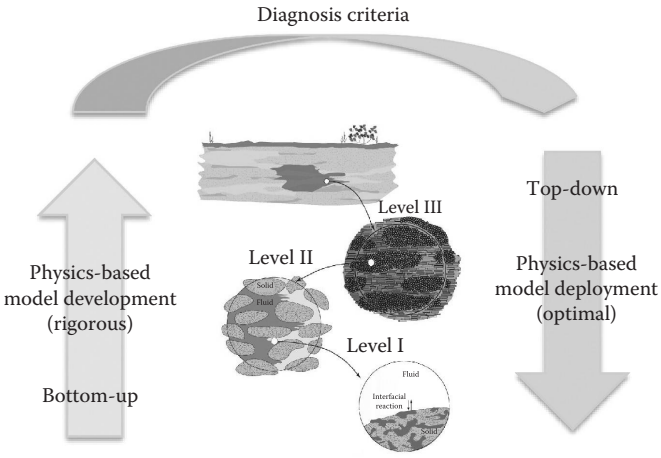

FIGURE 12.2 Conceptualization of the connection between *development* and *deployment* of physics-based multiscale models. The missing link between model development and deployment is generally the identification of diagnosis criteria to identify suitable models and modeling scales at which continuum-scale quantities and parameters are well defined. Hierarchy of scales inset (center). (Reproduced from Wood, B.D., *Adv. Water Resour.*, 32(5), 723, 2009.)

coupling conditions across multiple scales. However, it will not cover methods/approaches for scenarios where continuum models fail globally, that is, nonlocal models. We refer to [23] for a recent and thorough review on nonlocal models. In Section 12.2, we review some of the most common upscaling methods that allow one to derive macroscopic equations from their pore-scale counterparts. Classical results of homogenization theory are also presented. In Section 12.3, we discuss the upscaling of reactive systems with emphasis on the formulation of diagnosis criteria for the applicability of macroscopic models. Finally, Section 12.4 reviews multiscale approaches to modeling reactive transport systems with partial and/or total lack of spatial scale separation with an emphasis on hybrid multiscale schemes for reactive transport and discusses few test cases. The review will only touch upon the problem of temporal-scale separation and will highlight open questions in the field. Concluding remarks are presented in Section 12.5.

12.2 From First Principles to Effective-Medium Equations

Subsurface phenomena are amenable to mathematical descriptions on a multiplicity of scales that range from atomistic to continuum. Current modeling approaches can be subdivided into continuum (e.g., Darcy-, field-scale) and pore-scale models. Pore-scale models (e.g., Navier–Stokes equations), which describe transport processes with a high degree of fidelity, do not represent a viable alternative, as they are computationally prohibitive and impractical on the field scale since the pore-scale geometry is rarely known except for relatively small (e.g., tens of decimeters) lab samples. Macroscopic models (e.g., Darcy's law for fluid flow and an advection–dispersion equation for transport), which treat a porous medium as an "averaged" continuum, overcome these limitations by relying on phenomenological descriptions and a number of simplifications (e.g., spatial smoothness of pore-scale quantities, spatial periodicity of pore structures, and low degree of physical and chemical heterogeneity). This section presents an overview of common upscaling methods used to formally derive continuum-/Darcy-scale equations from pore-scale (mass, momentum and energy) conservation laws, and classical macroscale equations governing flow and tracer transport at the Darcy scale.

12.2.1 Classification of Upscaling Methods

We consider a multiphase system consisting of a solid matrix Ω_s and an interconnected fluid-filled pore space Ω_ℓ. We define $\Omega := \Omega_s \cup \Omega_\ell$ and call it a *porous medium*. The solid–liquid interface in Ω is denoted with $\mathcal{A}_{\ell s}$. A major goal of upscaling is to establish connections between pore- and continuum-scale descriptions of transport processes in Ω. Some of the mathematical approaches to upscaling include the method of volume averaging [24,25] and its modifications [26], generalizations of the method of moments [27–30], homogenization via multiple-scale expansions [31,32], pore-network models [33], and thermodynamically constrained averaging [34], just to mention a few. A comparison between different upscaling methods is discussed in [35,36]. A thorough overview on upscaling methods, including Martingale methods, stochastic approaches, and projection operators, is given in [37].

Let u be a real-valued scalar function that exhibits rapid spatial oscillations on a pore-scale domain Ω_ℓ. It describes a certain physical quantity and satisfies a partial differential equation,

$$\mathcal{L}\{u\} = f(u), \tag{12.1}$$

where $\mathcal{L}\{\cdot\}$ is a differential operator, for example, $\mathcal{L} = \partial_t + \mathbf{v}\cdot\nabla - D_0\nabla^2$. We emphasize that $\mathcal{L}\{\cdot\}$ can be nonlinear [38]. One can define the local average of u as

$$\langle u\rangle(\mathbf{x}) = \frac{1}{|\mathcal{V}|}\int_{\mathcal{V}(\mathbf{x})} u(\mathbf{y};\mathbf{x})\,\mathrm{d}\mathbf{y}\,, \tag{12.2}$$

where $\mathbf{x}$ is the centroid of the averaging volume $\mathcal{V}(\mathbf{x})$ and $\mathbf{y} \in \mathcal{V}(\mathbf{x})$. In the method of *volume averaging*, the support volume $\mathcal{V}$ "is a small, but not too small, neighborhood of point $\mathbf{x}$ of the size of a representative elementary volume (REV) (several hundred or thousand of pores)" [31, p. 1] (see inset in Figure 12.2). The ambiguity in defining the size of an REV is typical. For example, in [39, p. 15] "the size of the REV is defined by saying that it is

- Sufficiently large to contain a great number of pores so as to allow us to define a mean global property, while ensuring that the effects of the fluctuations from one pore to another are negligible (one may take, e.g., 1 cm^3 or 1 dm^3)
- Sufficiently small so that the parameter variations from one domain to the next may be approximated by continuous functions so that we may use infinitesimal calculus."

A discussion on the definition of REV can be found in [40]. A continuum-scale equation

$$\mathcal{L}^\star\{\langle u\rangle\} = g(\langle u\rangle), \tag{12.3}$$

is constructed by volumetric averaging (12.2) of the original pore-scale equation (12.1). The procedure is facilitated by the spatial averaging theorem, which enables one to exchange spatial integration and differentiation [24],

$$\langle\nabla u\rangle = \nabla\langle u\rangle + \frac{1}{|\mathcal{V}|}\int_{\Gamma(\mathbf{x})} u\mathbf{n}\,\mathrm{d}\mathbf{y}\,, \tag{12.4}$$

where $\Gamma(\mathbf{x})$ is the liquid–solid interface contained in $\mathcal{V}(\mathbf{x})$, that is, $\Gamma(\mathbf{x}) := \mathcal{A}_{\ell s} \cap \mathcal{V}(\mathbf{x})$, and $\mathbf{n}$ is the outward normal unit vector of Γ. A critical step in constructing a macroscopic approximation

(12.3) from (12.1) is to perform a Reynolds decomposition of pore-scale quantities within any $\mathcal{V}(\mathbf{x})$ with $\mathbf{x} \in \Omega$,

$$u(\mathbf{x}) = \langle u \rangle(\mathbf{x}) + \tilde{u}(\mathbf{x}), \tag{12.5}$$

where $\langle u \rangle(\mathbf{x})$ is the local average calculated in the centroid of the averaging volume and $\tilde{u}(\mathbf{x})$ a deviation from the average. Combining Reynolds decomposition (12.5) with the spatial averaging theorem (12.4) leads to

$$\langle \nabla u \rangle = \nabla \langle u \rangle + \frac{1}{|\mathcal{V}|} \int_{\Gamma(\mathbf{x})} \left[\langle u \rangle(\mathbf{y}) + \tilde{u}(\mathbf{y}) \right] \mathbf{n} \, \mathrm{d}\mathbf{y}, \quad \mathbf{y} \in \mathcal{V}(\mathbf{x}). \tag{12.6}$$

The previous form generally requires two main approximations: $\langle u \rangle(\mathbf{y}) \approx \langle u \rangle(\mathbf{x}) + \mathbf{y} \cdot \nabla \langle u \rangle(\mathbf{x}) + h.o.t.$ and $\tilde{u} \approx f(\langle u \rangle, \nabla \langle u \rangle, \ldots)$ referred to as localization and closure approximations, respectively. We emphasize that such approximations are necessary to fully decouple pore- and continuum-scale regardless of linearity/nonlinearity of the differential operator $\mathcal{L}$. The impact of such approximations on the applicability of single-point closure macroscopic approaches is discussed in Section 12.3. A reference book on the method of volume averaging is [24].

Similar concepts are used in *thermodynamically constrained averaging theory* [34], wherein thermodynamics is introduced into a constrained entropy inequality to guide the formation of closed macroscale models that retain consistency with microscale physics and thermodynamics.

In the *homogeneization theory* by multiple-scale expansions (see, e.g., [31]), the volume $\mathcal{V}$ is the unit cell of a periodic porous medium Ω with period ε. A homogenized equation is obtained by determining the following limit,

$$\langle u \rangle = \langle \lim_{\varepsilon \to 0} u_\varepsilon \rangle, \tag{12.7}$$

where u_ε is the sequence (indexed by ε) of solutions of Equation 12.1 with periodically oscillating coefficients. The limit is determined by utilizing a two-scale asymptotic expansion that "is an ansatz of the form,

$$u_\varepsilon(\mathbf{x}) = u_0(\mathbf{x}, \mathbf{x}/\varepsilon) + \varepsilon u_1(\mathbf{x}, \mathbf{x}/\varepsilon) + \varepsilon^2 u_2(\mathbf{x}, \mathbf{x}/\varepsilon) + \cdots, \tag{12.8}$$

where each function $u_i(\mathbf{x}, \mathbf{y})$ in this series depends on two variables, $\mathbf{x}$ the macroscopic (or slow) variable and $\mathbf{y}$ the microscopic (or fast) variable, and is $\mathcal{V}$-periodic in $\mathbf{y}$ ($\mathcal{V}$ is the unit period). A schematic of the procedure is provided in Figure 12.3. Inserting the ansatz (12.8) in Equation 12.1 satisfied by u_ε and identifying like-powers of ε leads to a cascade of equations for each term $u_i(\mathbf{x}, \mathbf{y})$. In general, averaging with respect to $\mathbf{y}$ yields the homogenized equation for u_0. Another step is required to rigorously justify the homogenization result obtained heuristically with this two-scale asymptotic expansion" [31, p. 238].

Similar to the homogenization theory definition of average is that of the *method of moments*, wherein the global ($\mathbf{x}$) and local

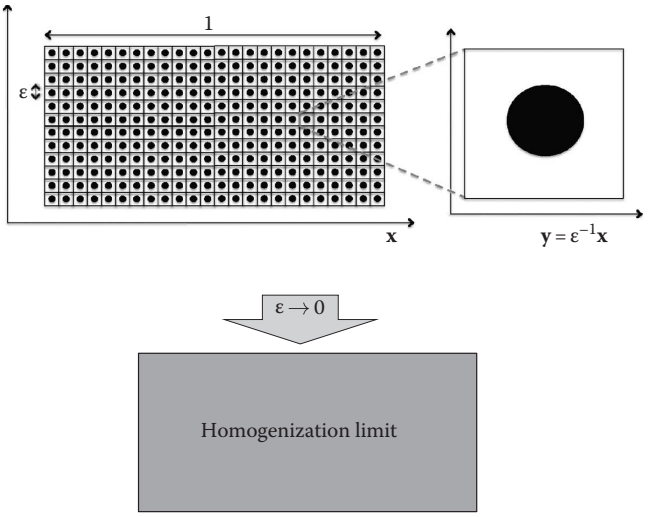

FIGURE 12.3 Schematics of a unit cell, the macroscopic domain and the homogenization to the continuum limit. The unit cell can be arbitrarily complex: it can contain multiple grains of arbitrary shapes.

($\mathbf{y}$) variables "characterize the instantaneous position (configuration) of the Brownian particle in its phase space. Together the vectors ($\mathbf{x}$, $\mathbf{y}$) define a multidimensional phase space $\mathbf{x} \oplus \mathbf{y}$ within which convective and diffusive solute-particle transport processes occur" [41, pp. 66–67]. In this case, a macroscopic transport equation is obtained for the probability density function of a Brownian particle [41, eq. 3.3–5]:

$$\overline{P}(\mathbf{x}, t \mid \mathbf{y}') \overset{def}{=} \int_{\mathcal{V}} P(\mathbf{x}, \mathbf{y}, t \mid \mathbf{y}') \mathrm{d}\mathbf{y}, \tag{12.9}$$

where $P(\mathbf{x}, \mathbf{y}, t|y') \equiv P(\mathbf{x}–\mathbf{x}', \mathbf{y}, t–t'|\mathbf{y}')$ with $\mathbf{x}' = 0$ and $t' = 0$ denotes the "conditional probability density that the Brownian particle is situated at position ($\mathbf{x}$, $\mathbf{y}$) at time t, given that it was initially introduced into the system at the position ($\mathbf{x}'$, $\mathbf{y}'$) at some earlier time t' ($t > t'$)" [41, p. 68]. "For sufficiently long times (i.e., 'long' relative to the time scale of evolution of the microscale transport process, but 'short' relative to the time scale of the macrotransport process) we expect that the particle(s) will loose memory of the initial position(s) $\mathbf{y}'$" [41, p. 91]. Consequently, $\overline{P}(\mathbf{x}, t \mid \mathbf{y}') \approx \overline{P}(\mathbf{x}, t)$ and a fully macrotransport equation can be determined.

A number of other approaches to upscaling are reviewed in [41]. Even if based on different definitions of the averaging volume and on distinct mathematical tools, all upscaling methods require *closure assumptions and localization approximations* to fully decouple the average system behavior from pore-scale information: the latter is exclusively incorporated into the upscaled equation through effective parameters that can be determined by laboratory experiments or numerical solution of a closure problem at the unit cell level.

Next, we present classical results from homogenization theory applied to flow and transport problems.

12.2.2 Momentum Transport: From Navier–Stokes to Darcy-Type Equations

Single-phase flow of an incompressible Newtonian fluid in the pore-space Ω_ℓ of a porous medium is described by the Stokes and continuity equations subject to the no-slip boundary condition on $\mathcal{A}_{\ell s}$:

$$\mu\nabla^2\mathbf{v} - \nabla p = 0, \quad \nabla\cdot\mathbf{v} = 0, \quad \mathbf{x}\in\Omega_\ell, \quad \mathbf{v} = 0, \quad \mathbf{x}\in\mathcal{A}_{\ell s}, \quad (12.10)$$

where $\mathbf{v}(\mathbf{x})$ is the fluid velocity, p denotes the fluid dynamic pressure, and μ is the dynamic viscosity.

Upscaling of the Stokes equations (12.10) at the pore scale to the continuum scale has been the subject of numerous investigations, including those relying on multiple-scale expansions [31,42–45, and references therein], volume averaging [46, and references therein], and the method of moments. These studies have demonstrated that Darcy's law, which was empirically established by Darcy in 1856 [47], and the continuity equation for $\langle\mathbf{v}\rangle$,

$$\langle\mathbf{v}\rangle = -\frac{\mathbf{K}}{\mu}\cdot\nabla\langle p\rangle, \quad \nabla\cdot\langle\mathbf{v}\rangle = 0, \quad \mathbf{x}\in\Omega, \quad (12.11)$$

provide an effective representation of the pore-scale Stokes flow (e.g., [31, Eq. 4.7]). Such upscaling procedures also enable one to formally define the permeability tensor $\mathbf{K}$ in Equation 12.11 as the average of a "closure variable" $\mathbf{k}(\mathbf{y})$, that is, $\mathbf{K} = \langle\mathbf{k}(\mathbf{y})\rangle$. The latter is the unique solution of a local problem (e.g., [31, pp. 46–47, Theorem 1.1] and [42, Eq. 22]) defined on a representative (unit) cell of the porous medium. "It is well admitted that the existence of continuum behaviors that are macroscopically equivalent to finely heterogeneous media needs a good separation of scales. If ℓ and L are the characteristic lengths at the local and the macroscopic scale, respectively, their ratio should obey" [48]

$$\varepsilon = \frac{\ell}{L} \ll 1. \quad (12.12)$$

To describe flow through "hyperporous" media, Brinkman [49] introduced a modification of Darcy's law,

$$\nabla\langle p\rangle = -\frac{\mu}{\mathbf{K}}\langle\mathbf{v}\rangle + \mu_e\nabla^2\langle\mathbf{v}\rangle, \quad (12.13)$$

where μ_e is an effective viscosity "which may differ from μ" [49]. The *raison d'etre* for such a modification was the necessity of obtaining an equation that was valid in the high permeability limit ($|\mathbf{K}|\to\infty$) and that allowed for a direct coupling with the Stokes equations at interfaces separating Stokes flow (infinite permeability regions) and filtration flow (low permeability regions). In Brinkman's words, "this equation has the advantage of approximating (12.11) for low values of $\mathbf{K}$ and (12.10) for high values of $\mathbf{K}$."

After its introduction and its widespread use, an increasing research effort was devoted to the identification of domains of validity of both Darcy's and Brinkman's law [28,50,51, and references therein]. Brinkman's intuition was mathematically proven later by Goyeau et al. [52] and Auriault et al. [48], who used, respectively, the method of volume averaging and multiple-scale expansions to demonstrate that Brinkman's equation represents a higher-order approximation of Darcy's law when the separation of scales is poor. Poor-scale separation can be encountered in two typical situations.

> The first one occurs when the porous medium is macroscopically heterogeneous, when the macroscopic characteristic length L associated to the macroscopic heterogeneities is not very large compared to the characteristic length ℓ of the pores. For such media, length L can be estimated by $L \approx K/|\nabla K|$, where K is the permeability. When the macroscopic gradient of the permeability $|\nabla K|$ is large, the ratio ℓ/L may not be very small and the separation of scale is poor. The second typical situation corresponds to large gradients of pressure which are applied to macroscopically homogeneous media. The macroscopic characteristic length $L \approx p/|\nabla p|$ associated to this gradient of pressure could be not very large compared to ℓ [48].

In a subsequent work, Auriault [51] defines the applicability range of Darcy's and Brinkman's equations in terms of the geometric parameters of three classes of porous media: classical porous media characterized by connected porous matrix (e.g., capillary tubes), swarms of fixed particles with connected pore space, and fibrous media. It is finally concluded that the validity domain of Brinkman's equation corresponds to porous media with very large porosity and very small solid concentration.

Darcy and Brinkman equations have been demonstrated to be quite accurate in describing macroscopic momentum transfer at low Reynolds numbers for scales ranging from the nanometer to the field scale in a variety of engineering [53–55], hydrology, and ecohydrology applications [56–58], just to mention a few (see [59] for a review). The Forchheimer equation (e.g., [60,61]) and its generalizations allow one to include inertia and turbulence effects in the momentum balance [60,62].

Knowledge of the flow field allows one to study transport processes at any given scale as described in the following section.

12.2.3 Mass Transport: From Diffusion to Dispersion Equations

The body of literature on upscaling reactive and nonreactive transport is extremely rich and its complete review is beyond the scope of this section. Instead, we focus on a standard transport scenario for the purpose of illustration only. Let us assume that the fluid contains a dissolved species $\mathcal{M}$, whose molar concentration $c(\mathbf{x}, t)$ [mol L^{-3}] at point $\mathbf{x}\in\Omega_\ell$ and time $t > 0$ changes

due to advection, molecular diffusion, homogeneous reaction in the liquid phase, and heterogeneous reaction at the solid–liquid interface $\mathcal{A}_{\ell s}$. At the pore scale, the first three phenomena are described by an advection–diffusion–reaction equation,

$$\frac{\partial c}{\partial t} + \mathbf{v} \cdot \nabla c = \nabla \cdot (\mathbf{D} \nabla c) + R(c), \quad \mathbf{x} \in \Omega_\ell, \quad t > 0, \quad (12.14)$$

where the molecular diffusion coefficient $\mathbf{D}$ is, in general, a positive-definite second-rank tensor. If diffusion is isotropic, $\mathbf{D} = \mathscr{D}_0 \mathbf{I}$ where $\mathscr{D}_0$ [L^2T^{-1}] is the diffusion coefficient and $\mathbf{I}$ is the identity matrix. The source term $R(c)$ represents a generic homogeneous reaction. At the solid–liquid interface $\mathcal{A}_{\ell s}$ impermeable to flow, mass conservation requires that mass flux of the species $\mathcal{M}$ be balanced by the net mass flux due to the heterogeneous reaction, $Q(c)$:

$$-\mathbf{n} \cdot \mathbf{D} \nabla c = Q(c), \quad \mathbf{x} \in \mathcal{A}_{\ell s}. \quad (12.15)$$

In addition to Equation 12.15, flow and transport equations (12.10) and (12.14) are supplemented with boundary conditions on the external boundary of the flow domain Ω. Regardless of the specific upscaling method employed, the upscaling of Equations 12.14 and 12.15 leads to effective equations for the average concentration $\langle c \rangle$,

$$\frac{\partial \langle c \rangle}{\partial t} + \langle \mathbf{v} \rangle \cdot \nabla \langle c \rangle = \nabla \cdot (\mathbf{D}^* \cdot \nabla \langle c \rangle) + \mathcal{R}(\langle c \rangle) + \mathcal{Q}(\langle c \rangle), \quad \mathbf{x} \in \Omega, \quad t > 0, \quad (12.16)$$

where $\mathbf{D}^*$ is the macroscopic dispersion tensor, and $\mathcal{R}(\langle c \rangle)$ and $\mathcal{Q}(\langle c \rangle)$ are effective reaction terms modeling homogeneous and heterogeneous reactions, respectively.

It is worth emphasizing that, since $\langle R(c) \rangle \neq R(\langle c \rangle)$ and $\langle Q(c) \rangle \neq Q(\langle c \rangle)$, in general $\mathcal{R} \neq R(\langle c \rangle)$ and $\mathcal{Q} \neq Q(\langle c \rangle)$ regardless whether or not R and Q are linear. The upscaling of advective–reactive pore-scale transport to advection–reaction–dispersion equations of the type (12.16) for different functional forms of the reaction rates has been the focus of an incredibly large number of studies. In these, virtually any upscaling method available has been used to derive the macrotransport equations. Recent studies on the topic include [35,63–66], just to mention a few. There are also numerous generalizations to include multicomponent reactive system with linear/nonlinear homogeneous and heterogeneous (bio)reactions and various functional forms of $R(c)$ and $Q(c)$ relevant to engineering, chemical, biochemical, hydrological, and other applications, for example, [27,29,30,67–71]. Further, while generally determined by fitting a solution of the dispersion equation to data, the dispersion tensor $\mathbf{D}^*$ can be formally related to a solution of a closure problem in the REV (in volume averaging) or unit cell (in homogenization technique) [65]. Solving a closure problem in the REV or in the unit cell has the advantage of predictively relating pore-scale dynamics and geometry to macroscopic coefficients. Yet, such an approach has failed to describe transport processes in systems with slight departures from highly idealized scenarios. This is due firstly to the difficulty of identifying an appropriate unit cell/REV in real rocks and soils and, secondly, to the failure of some of the approximations and assumptions (i.e., localization approximation and closure) necessary to fully decouple macroscopic equations from their pore-scale counterparts. Nonlocal models, far beyond the scope of this review, overcome some of the limitations of the localization approximation through space-time convolution integrals, fractional derivatives, etc. [63,72,73]. The identification of the applicability conditions of upscaled models based on closure assumptions has drawn much less attention. This knowledge is critical to ensure model robustness and predictivity and to bound modeling errors. This will be the focus of the following section.

12.3 Robustness of Macroscopic Models

While useful in a variety of applications, local continuum models (e.g., advection–dispersion–reaction equations or ADREs) fail to capture experimentally observed macroscopic transport features, including scale dependence of dispersion tensor [74] and reaction coefficients [75], non-Gaussian plumes, macroscale mixing [76], and the onset of instability in variable density flows [77], to cite a few. ADRE-based models of transport of (bio)chemically reactive solutes, which are the main focus of this chapter, can significantly overpredict the extent of reactions in mixing-induced chemical transformations [69,75,78–80, and references therein]. These and other shortcomings stem from the inadequacy of either standard macroscopic models or their parametrizations or both.

Upscaling from the pore scale, on which governing equations are physically based and well defined, to the continuum scale, on which they are used for both quantitative and qualitative predictions, often enables one to establish the connection between the two modeling scales. In particular, upscaling approaches that rely on characteristic dimensionless numbers (e.g., the Damköhler and Péclet numbers) can provide quantitative measures for the validity of various upscaling approximations.

12.3.1 Diagnosis Criteria for Darcy-Scale Models Breakdown

Criteria under which classical macroscopic models accurately represent, and are predictive of, pore-scale processes have been investigated throughout the years. Auriault and Adler [42] first used multiple-scale expansions to establish the applicability range of an advection–dispersion equation for tracers in terms of Péclet number. Mikelić et al. [43] provided a rigorous upscaled version of the Taylor dispersion problem with linear heterogeneous reaction. For flow between two parallel reacting plates, they established the applicability range of the upscaled equation in terms of Damköhler and Peclét numbers. Experimentally, [81] investigated how different existing macroscopic models for

diffusive mass transfer could or could not fit the breakthrough curves of double-permeability media for different values of Damköhler and Peclét numbers.

Nonlinearity of governing equations complicates the upscaling of most reactive transport phenomena. It requires a linearization and/or other approximations, whose accuracy and validity cannot be ascertained a priori. This is especially so for a large class of transport processes, such as mixing-induced precipitation, which exhibit highly localized reacting fronts and consequently defy macroscopic descriptions that are completely decoupled from their microscopic counterparts [26,42,67].

12.3.1.1 Dimensionless Formulation

Upscaling approaches that rely on characteristic dimensionless numbers (e.g., the Damköhler and Péclet numbers) can provide quantitative measures for the validity of various upscaling approximations [82–84]. In the following, we illustrate a general approach based on the multiple-scale expansion technique applied to dimensionless transport equations. It is suited to identifying applicability conditions of any given macroscopic equations. This approach allows one to gain physical insight of pore-scale processes and their local macroscopic manifestation, if it exists.

Let us start with Equation 12.14, where we set $R(c) = 0$ and $Q(c) = k(c^a - \overline{c}^a)$, without loss of generality. Here, k, $\overline{c}$, and a are the reaction rate, the equilibrium concentration at the pore scale, and the order of reaction, respectively. Let us introduce the dimensionless quantities

$$\hat{c} = \frac{c}{\overline{c}}, \quad \hat{\mathbf{x}} = \frac{\mathbf{x}}{L}, \quad \hat{\mathbf{v}} = \frac{\mathbf{v}}{U}, \quad \hat{\mathbf{D}} = \frac{\mathbf{D}}{D}, \quad \hat{p} = \frac{p\ell^2}{\nu UL}, \tag{12.17}$$

where D and U are characteristic values of $\mathbf{D}$ and $\mathbf{v}$, respectively, and ε is defined by Equation 12.12. Further, we define characteristic diffusion, reaction, and advection time scales, t_d, t_r, and t_a. Péclet (Pe_1) and Damköhler (Da_1) numbers are defined as the ratio between diffusion (t_d) and advection (t_a) or reaction t_r time scales, respectively. Specifically,

$$\mathrm{Da}_1 := \frac{t_d}{t_r} = \frac{Lk\overline{c}^{a-1}}{D}, \quad \text{and} \quad \mathrm{Pe}_1 := \frac{t_d}{t_a} = \frac{UL}{D}. \tag{12.18}$$

Rewriting Equations 12.10 and 12.14 in terms of the dimensionless quantities (12.17) and the dimensionless time $\hat{t} = t/t_d$ yields a dimensionless form of the flow equation in the fluid domain $\mathcal{B}$ of the unit cell Y (see Figure 12.3),

$$\varepsilon^2\hat{\nabla}^2\hat{\mathbf{v}} - \nabla\hat{p} = 0, \quad \hat{\nabla}\cdot\hat{\mathbf{v}} = 0, \tag{12.19}$$

subject to the no-slip boundary condition $\hat{\mathbf{v}} = 0$ on the grain–liquid interface, Γ, and a dimensionless form of the transport equation in the fluid domain,

$$\frac{\partial\hat{c}}{\partial\hat{t}} + \hat{\nabla}\cdot(-\hat{\mathbf{D}}\hat{\nabla}\hat{c} + \mathrm{Pe}_1\hat{\mathbf{v}}\hat{c}) = 0, \tag{12.20}$$

subject to

$$-\mathbf{n}\cdot\hat{\mathbf{D}}\hat{\nabla}\hat{c} = \mathrm{Da}_1(\hat{c}^a - 1), \quad \hat{\mathbf{x}} \in \Gamma. \tag{12.21}$$

For the sake of simplicity, we will drop the hatted notation $(\hat{\cdot})$.

12.3.1.2 Homogenization via Multiple-Scale Expansions

The method of multiple-scale expansions is based on the ansatz that any (dimensionless) pore-scale quantity can be expanded into an asymptotic series in powers of ε, for example,

$$c(\mathbf{x},\mathbf{y},t,\tau_r,\tau_a) = \sum_{m=0}^{\infty}\varepsilon^m c_m(\mathbf{x},\mathbf{y},t,\tau_r,\tau_a), \tag{12.22}$$

where $\mathbf{y}$ is a fast space variable, τ_r and τ_a are two time variables,

$$\mathbf{y} = \frac{\mathbf{x}}{\varepsilon}, \quad \tau_r = \mathrm{Da}_1 t, \quad \tau_a = \mathrm{Pe}_1 t, \tag{12.23}$$

and $c_m(\mathbf{x}, \mathbf{y}, t, \tau_r, \tau_a)$ ($m = 0,1,\ldots$) are Y-periodic in $\mathbf{y}$, that is, periodic in $\mathbf{y}$ with period Y. In Equation 12.23, we set

$$\mathrm{Pe}_1 = \varepsilon^{-\alpha}, \quad \mathrm{Da}_1 = \varepsilon^{\beta}, \tag{12.24}$$

with the exponents α and β determining the system behavior. For example, if $\mathrm{Pe}_1 \gg 1$ (or $\alpha > 0$) and $\mathrm{Da}_1 \gg 1$ (or $\beta < 0$) then advection and reaction dominate diffusion at the pore scale, respectively. Substitution of Equations 12.22 through 12.24 in Equation 12.20 (and Equation 12.19), while matching ε-like orders, leads to a cascade of equations for c_0, c_1, etc. At the leading order $\mathcal{O}(\varepsilon^{-2})$, one obtains [83, (A.9)]

$$c_0 = c_0(\mathbf{x},t,\tau_r,\tau_a). \tag{12.25}$$

At the order $\mathcal{O}(\varepsilon^{-1})$, a solution for c_1 can be written in the form

$$c_1(\mathbf{x},\mathbf{y},t,\tau_r,\tau_a) = \boldsymbol{\chi}(\mathbf{y})\cdot\nabla_{\mathbf{x}}c_0(\mathbf{x},t,\tau_r,\tau_a) + \overline{c}_1(\mathbf{x},t,\tau_r,\tau_a), \tag{12.26}$$

where $\overline{c}_1$ is an integration function and the closure variable $\boldsymbol{\chi}(\mathbf{y})$ satisfies the boundary value problem

$$\begin{aligned}&\left[-\nabla_{\mathbf{y}}\cdot\mathbf{D}(\nabla_{\mathbf{y}}\boldsymbol{\chi} + \mathbf{I}) + \varepsilon^{1-\alpha}\mathbf{v}_0\cdot\nabla_{\mathbf{y}}\boldsymbol{\chi}\right]\cdot\nabla_{\mathbf{x}}c_0 \\ &\quad = \varepsilon^{1-\alpha}(\phi^{-1}\langle\mathbf{v}_0\rangle - \mathbf{v}_0)\cdot\nabla_{\mathbf{x}}c_0 + \varepsilon^{\beta}\mathcal{K}^*\left(c_0^a - 1\right),\end{aligned} \tag{12.27}$$

for $\mathbf{y} \in \mathcal{B}$ subject to $\langle\chi\rangle = 0$ subject to

$$-[\mathbf{n}\cdot\mathbf{D}(\nabla_{\mathbf{y}}\boldsymbol{\chi} + \mathbf{I})]\cdot\nabla_x c_0 = \varepsilon^{\beta}\left(c_0^a - 1\right), \quad \mathbf{y} \in \Gamma, \tag{12.28}$$

where

$$\phi = \frac{|\mathcal{B}|}{|Y|} \quad \text{and} \quad \mathcal{K}^\star = \frac{|\Gamma|}{|\mathcal{B}|}, \tag{12.29}$$

are porosity and the effective reaction rate, respectively. The boundary value problem (12.27) and (12.28) couples the pore scale with the continuum scale since χ is influenced by the continuum scale through the macroscale quantity $c_0(\mathbf{x})$ and its gradients. This is incompatible with the hypothesis that χ should be only function of $\mathbf{y}$. This inconsistency is resolved by imposing appropriate conditions on α and β as outlined in the following.

12.3.1.3 Macroscopic Equations and Applicability Regimes

The selection of proper α and β ensures that χ is independent of c_0, that is, $\chi(\mathbf{y})$. In particular, if we chose $\beta > 0$ in the boundary condition (12.28), then the right-hand side (RHS), which is of order ε^β, can be neglected since $\varepsilon \ll 1$. Next, we observe that for the term $\varepsilon^\beta \mathcal{K}^\star \left(c_0^a - 1\right)$ to be negligible relative to the smallest term in Equation 12.27, it is necessary that $\beta > \max\{0, 1-\alpha\}$. Since homogenizability of pore-scale advection–diffusion transport of a conservative solute requires that $\alpha < 2$ [42, Sec. 3.5, Tab. 1], this condition yields either $\beta + \alpha > 1$ if $\alpha < 1$ or $\beta > 0$ if $1 < \alpha < 2$. Therefore, the dependence of χ on $\nabla_{\mathbf{x}} c_0$ is eliminated by defining χ as a solution of the simplified cell problem

$$-\nabla_{\mathbf{y}} \cdot \mathbf{D}(\nabla_{\mathbf{y}} \chi + \mathbf{I}) + \varepsilon \mathrm{Pe}_1 \mathbf{v}_0 \nabla_{\mathbf{y}} \chi = \varepsilon \mathrm{Pe}_1 (\langle \mathbf{v}_0 \rangle_{\mathcal{B}} - \mathbf{v}_0), \quad \mathbf{y} \in \mathcal{B}, \tag{12.30}$$

$$-\mathbf{n} \cdot \mathbf{D}(\nabla_{\mathbf{y}} \chi + \mathbf{I}) = 0, \quad y \in \Gamma, \tag{12.31}$$

when the following conditions on the order of magnitude of Da_1 and Pe_1 are satisfied [83]:

$$\mathrm{Pe}_1 < \varepsilon^{-2}, \quad \frac{\mathrm{Da}_1}{\mathrm{Pe}_1} < \varepsilon, \quad \mathrm{Da}_1 < 1. \tag{12.32}$$

Under these conditions, the (sub)pore-scale reactive transport described by Equation 12.20 can be homogenized, that is, *approximated up to order* ε^2, with an effective ADRE

$$\phi \partial_t \langle c \rangle = \nabla \cdot (\mathbf{D}^\star \nabla \langle c \rangle - \phi \mathrm{Pe}_1 \langle \mathbf{v} \rangle \langle c \rangle) - \varepsilon^{-1} \phi \mathrm{Da}_1 \mathcal{K}^\star (\langle c \rangle^a - 1), \tag{12.33}$$

where $\langle c \rangle = \langle c_0 \rangle + \varepsilon \langle c_1 \rangle + \mathcal{O}(\varepsilon^2)$ is the spatially averaged concentration over a unit cell Y, and $\varepsilon \ll 1$ is the separation of scale parameter, that is, the ratio between characteristic spatial scales at the (sub)pore and continuum levels [83]. We emphasize that since Pe_1 and Da_1 are bounded according to Equation 12.32, the reaction term will not dominate dispersion. In Equation 12.33, $\mathcal{K}^\star$ and ϕ are the effective reaction rate and porosity, defined in Equation 12.29, and

$$\mathbf{D}^\star = \langle \mathbf{D}(I + \nabla_{\mathbf{y}} \chi) \rangle + \varepsilon Pe_1 \langle \chi \mathbf{k} \rangle \nabla_{\mathbf{x}} p_0 \tag{12.34}$$

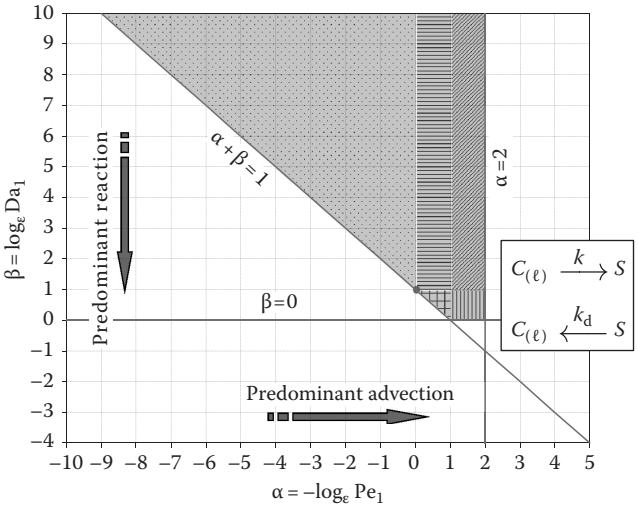

FIGURE 12.4 Phase diagram indicating the range of applicability of macroscopic equations for a single component advection–reaction–diffusion system in terms of Péclet (Pe_1) and Damköhler (Da_1) numbers [83]. The gray region identifies the sufficient conditions under which the macroscopic equations hold. In the white region, macro- and microscale problems are coupled and have to be solved simultaneously. The different patterns identify different transport regimes depending on the order of magnitude of Pe_1 and Da_1.

is the dispersion tensor. In Equation 12.34, $\mathbf{k}$ can be determined as the solution of a closure problem for the flow in the unit cell Y (details can be found in [83, Eq. 17]).

Conditions (12.32) impose explicit constraints on transport processes that admit an accurate effective-medium description (i.e., errors bounded by ε). The region of validity of ADRE (12.33) is fully described by a phase diagram in the (Da_1,Pe_1)-space: the gray region in Figure 12.4 represents a parameter subspace where the former constraints are satisfied, while the white area indicates a set of transport processes that violate such bounds. The robustness of these constraints has been recently and independently verified through 3D pore-scale direct numerical simulations of calcite dissolution [85].

The phase diagram reveals that transport phenomena dominated at the (sub)pore scale by reaction and/or advective processes do not lend themselves to macroscopic (upscaled) descriptions. These physical processes lead to high concentration gradients, that is, reactive fronts, at the (sub)pore scale, which are not suitable for accurate representation in terms of averaged quantities. Under these conditions, the accuracy of ADREs, such as Equation 12.33, cannot be ascertained a priori. Phase diagrams of the type showed in Figure 12.4 can be used to estimate various upscaling approximations.

12.3.2 Adaptive Diagnosis Criteria for Algorithm Refinement

Reactive transport in the subsurface, for example, complexation reactions, generally involve very complex multicomponent

reaction networks. The approach described in Section 12.3.1 to obtain conditions under which classical local macroscopic models can accurately describe pore-scale processes has the advantage of generality. As a result, generalization to multicomponent reactions is relatively straightforward. However, the applicability conditions as formulated in Equation 12.32 are of limited practical use since they do not provide spatial and temporal adaptivity criteria, that is, they do not provide any information of where and when continuum-scale models are invalidated. In this section, we present and formulate adaptive diagnosis criteria for algorithm refinement based on continuum-scale functionals for a more realistic reactive system involving three reactive solutes (*A*, *B*, and *C*).

12.3.2.1 Applicability Conditions for Multicomponent Reactive Systems

Let species *A* and *B* undergo a nonlinear homogeneous reaction, and species *C* precipitates on the solid matrix, that is,

$$A_{(\ell)} + B_{(\ell)} \underset{k_c}{\overset{k_{ab}}{\rightleftarrows}} C_{(\ell)} \underset{k_d}{\overset{k}{\rightleftarrows}} S\,. \tag{12.35}$$

The system behavior is fully controlled by the Péclet (Pe_1) and three Damköhler (Da_j, $j = \{1,2,3\}$) numbers, which quantify the relative importance of the four key mechanisms involved in the transport process, that is, advection, molecular diffusion, homogeneous, and heterogeneous reactions. In particular, Pe_1 and Da_1 are defined in Equation 12.18. Additionally,

$$\mathrm{Da}_2 = \frac{L^2 k_{ab}}{\mathcal{D}_0} a_\star, \quad \text{and} \quad \mathrm{Da}_3 = \frac{L^2 k_c}{\mathcal{D}_0}, \tag{12.36}$$

where $a_\star$ is a characteristic concentration value of the reactants *A* and *B*. Also,

$$\mathrm{Da}_2 = \varepsilon^{\delta} \quad \text{and} \quad \mathrm{Da}_3 = \varepsilon^{\gamma}\,. \tag{12.37}$$

At the pore scale, the transport equations for the dimensionless concentrations *a*, *b*, and *c* are

$$\partial_t a + \nabla\cdot(-\mathbf{D}\nabla a + \mathrm{Pe}_1 \mathbf{v} a) = -\mathrm{Da}_2 ab + \eta \mathrm{Da}_3 c, \tag{12.38}$$

$$\partial_t b + \nabla\cdot(-\mathbf{D}\nabla b + \mathrm{Pe}_1 \mathbf{v} b) = -\mathrm{Da}_2 ab + \eta \mathrm{Da}_3 c, \tag{12.39}$$

$$\partial_t c + \nabla\cdot(-\mathbf{D}\nabla c + \mathrm{Pe}_1 \mathbf{v} c) = \eta^{\,1}\mathrm{Da}_2 ab - \mathrm{Da}_3 c\,, \tag{12.40}$$

where $\eta = \overline{c}/a_\star$ and $\overline{c}$ is the equilibrium concentration at the pore scale. The system (12.38) through (12.40) is subject to

$$\mathbf{n}\cdot\mathbf{D}\nabla a = \mathbf{n}\cdot\mathbf{D}\nabla b = 0, \quad -\mathbf{n}\cdot\mathbf{D}\nabla c = \mathrm{Da}_1(c^a - 1), \quad \mathbf{x}\in\Gamma, \quad t > 0\,. \tag{12.41}$$

Following a similar procedure to that outlined in the previous section, the pore-scale reactive transport processes described by Equations 12.38 through 12.41 can be homogenized, that is, approximated up to order ε^2, with an effective ADRE

$$\begin{aligned}
\phi\frac{\partial\langle a\rangle}{\partial t} &= \nabla\cdot(\mathbf{D}^*\nabla\langle a\rangle - \mathrm{Pe}\langle a\rangle\langle\mathbf{v}\rangle) - \phi\mathrm{Da}_2\langle a\rangle\langle b\rangle + \phi\eta\mathrm{Da}_3\langle c\rangle,\\
\phi\frac{\partial\langle b\rangle}{\partial t} &= \nabla\cdot(\mathbf{D}^*\nabla\langle b\rangle - \mathrm{Pe}\langle b\rangle\langle\mathbf{v}\rangle) - \phi\mathrm{Da}_2\langle a\rangle\langle b\rangle + \phi\eta\mathrm{Da}_3\langle c\rangle,\\
\phi\frac{\partial\langle c\rangle}{\partial t} &= \nabla\cdot(\mathbf{D}^*\nabla\langle c\rangle - \mathrm{Pe}\langle c\rangle\langle\mathbf{v}\rangle) + \phi\eta^{-1}\mathrm{Da}_2\langle a\rangle\langle b\rangle\\
&\quad - \phi\mathrm{Da}_3\langle c\rangle, \quad -\varepsilon^{-1}\phi\mathrm{Da}_1\mathcal{K}^\star(\langle c\rangle^a - 1),
\end{aligned} \tag{12.42}$$

if the following conditions are satisfied

$$\frac{\mathrm{Da}_i}{\mathrm{Pe}} < \varepsilon^{-1} \quad \text{and} \quad \mathrm{Da}_i < \varepsilon^{-2}, \quad i = \{2,3\}, \tag{12.43}$$

in addition to the bounds (12.32). The result is a higher dimensional phase diagram sketched in Figure 12.5 [84].

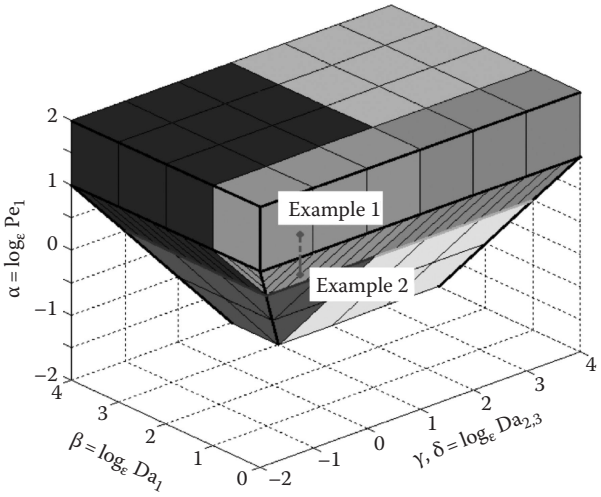

FIGURE 12.5 Phase diagram indicating the range of applicability of macroscopic equations for the advection–reaction–diffusion system (12.38) through (12.41) in terms of Pe and Da_j(j = {1,2,3}). The grey-scale region identifies the sufficient conditions under which the macroscopic equations hold. In the white region, macro- and microscale problems are coupled and have to be solved simultaneously. The colors identify different transport regimes depending on the order of magnitude of Pe and Da_j. (Adapted from Boso, F. and Battiato, I., *Adv. Water Resour.*, 62, 254, 2013.)

12.3.2.2 Numerical Tests

Numerical simulations, both at the pore- and macroscale, can be employed to test the robustness of sufficient conditions (12.32) and (12.43), or the phase diagram in Figure 12.5. For the sake of simplicity, let us consider a pressure-driven flow through a bidimensional fracture $\Omega = \{(x, y)\colon x \in (0, 1), |y| \le \varepsilon\}$ of width 2ε and unitary length, with solid boundary $\Gamma = \{(x, y)\colon x \in (0, 1), y = \pm\varepsilon\}$ (see Figure 12.6a). We assume that the precipitation/dissolution process does not significantly affect the interface Γ, and the

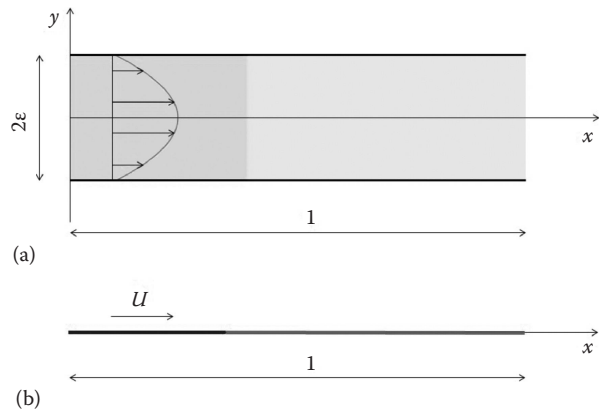

FIGURE 12.6 Sketch of the simulation domains where all the spatial scales are nondimensionalized by L, the fracture length. (a) Pore-scale (2D) fracture with fully developed parabolic velocity profile. Species A (in red) and B (in blue) occupy the left and right portion of the fracture, respectively. The reaction front is localized in the fracture center. (b) Macroscopic (1D) representation of the fracture. (Adapted from Boso, F. and Battiato, I., *Adv. Water Resour.*, 62, 254, 2013.)

evolution of the solid–liquid boundary needs not to be taken into account. For a fracture of width H, the length L is to be interpreted as the "observation scale" [43]. In all the numerical simulations, $\varepsilon := H/L = 6.25 \times 10^{-3}$ and $a = 1$.

Two test cases are considered: their parameter values are listed in Table 12.1. Example 1 satisfies all the constraints (12.32) and (12.43), while Example 2 violates one or more conditions for homogenizability. For each scenario, macroscale concentration profiles along the fracture $\langle\psi\rangle_M$, $\psi = \{a,b,c\}$, obtained by solving the continuum-scale system (12.42), are compared with the spatially averaged microscale concentration fields $\langle\psi\rangle_m$ calculated by numerical integration of pore-scale concentration profiles ψ according to $\langle\psi\rangle_m = (2\varepsilon)^{-1}\int_{-\varepsilon}^{\varepsilon}\psi(x,y)\mathrm{d}y$. Inside the homogenizability region, the solution of Equation 12.42 is expected to be within errors $\mathcal{O}(\varepsilon^2)$ from the averaged pore-scale solution, that is, $\langle\psi\rangle_m = \langle\psi\rangle_M + \mathcal{O}(\varepsilon^2)$, or the absolute error $E_\psi = |\langle\psi\rangle_m - \langle\psi\rangle_M| \approx \mathcal{O}(\varepsilon^2)$.

In Figure 12.7, we present a scenario of multicomponent reactive transport (described by Equation 12.35) through a planar fracture where the second of the applicability conditions (12.32) is violated (Test Case 3 of [84]). For such a scenario (Example 2), the continuum-scale solution is not able to describe pore-scale processes within the *expected* accuracy, that is, the accuracy prescribed by the upscaling procedure. Instead, when no conditions are violated (Example 1, Figure 12.8), the errors are bounded by ε, as predicted by homogenization theory [84, Test Cases 1 and 2]. *This suggests that the constraints derived through homogenization are robust in identifying sufficient as well as necessary conditions for homogenizability.*

TABLE 12.1 List of Parameters for Examples 1 and 2, Inside and Outside of the Applicability Regimes, Respectively

	Example 1	Example 2
α	1	1/2
β	1/4	1/4
γ	−1	−1
δ	−1	−1
$\alpha+\beta$	5/4	**3/4**
$\alpha+\gamma$	0	−1/2
$\alpha+\delta$	0	−1/2

Note: The boldface notation indicates the constraints that has been violated.

12.3.2.3 Adaptive Diagnosis Criteria for Multicomponent Reactive Systems

The applicability conditions identified by Equations 12.32 and 12.43 are not space-time dependent, that is, for any prescribed reaction network and physical system, Pe_1 and Da_i, $i = \{1,2,3\}$, are fixed. Instead, we define modified $\overline{\mathrm{Pe}_1}$ and $\overline{\mathrm{Da}_1}$ based on continuum-scale velocity and concentration, that is,

$$\overline{\mathrm{Pe}_1}(\mathbf{x}) = \frac{L}{D_0}\langle\mathbf{v}\rangle(\mathbf{x}) \quad \text{and} \quad \overline{\mathrm{Da}_1}(\mathbf{x},t) = \frac{Lk}{D_0}\langle c\rangle^{a-1}(\mathbf{x},t). \tag{12.44}$$

We emphasize that in Equation 12.44 both macroscale velocity and concentration are dimensional. If the exponent $a = 1$, $\overline{\mathrm{Da}_1}(\mathbf{x}, t)$ can be defined in terms of the dimensionless macroscale concentration instead. If at least one of the following inequalities,

$$\overline{\mathrm{Pe}_1}(\mathbf{x},t) > \varepsilon^{-2} \quad \text{or} \quad \frac{\overline{\mathrm{Da}_1}(\mathbf{x},t)}{\overline{\mathrm{Pe}_1}(\mathbf{x},t)} > \varepsilon \quad \text{or} \quad \overline{\mathrm{Da}_1}(\mathbf{x},t) > 1, \tag{12.45}$$

is satisfied at any space-time location $(\mathbf{x}, t)$, then at least one of the constraints (12.32) is violated, since $\langle\mathbf{v}\rangle(\mathbf{x}) \le \mathbf{v}(\mathbf{y};\mathbf{x})$ and $\langle c\rangle(\mathbf{x}, t) \le c(\mathbf{y}, t;\mathbf{x})$ for any $\mathbf{y} \in \mathcal{V}(\mathbf{x})$. The constraints (12.45) provide rigorous time-space dependent criteria to identify regions in a computational domain, where local breakdown of ADRE may occur, the ADRE solution may not be accurate and pore-scale models should be used instead. The bounds (12.45) can be straightforwardly generalized to multicomponent reactive transport for any specific reactive system of interest. For the reacting system described by Equation 12.35, the following conditions (in addition to Equation 12.45) must be verified for an algorithm refinement (i.e., the employment of a more accurate model such as pore-scale simulations) to take place

$$\frac{\overline{\mathrm{Da}_i}(\mathbf{x},t)}{\overline{\mathrm{Pe}_1}(\mathbf{x},t)} > \varepsilon^{-1} \quad \text{or} \quad \overline{\mathrm{Da}_i}(\mathbf{x},t) > \varepsilon^{-2}, \quad i = \{2,3\}, \tag{12.46}$$

where, for example, $\overline{\mathrm{Da}_2} = L^2 k_{ab}\langle a\rangle(\mathbf{x}, t)/D_0$ and $\overline{\mathrm{Da}_3} = L^2 k_c\langle c\rangle(\mathbf{x},t)/D_0$. We employ the proposed adaptivity criteria to the test case for the multicomponent reactive transport problem, presented earlier, where the continuum-scale model fails globally

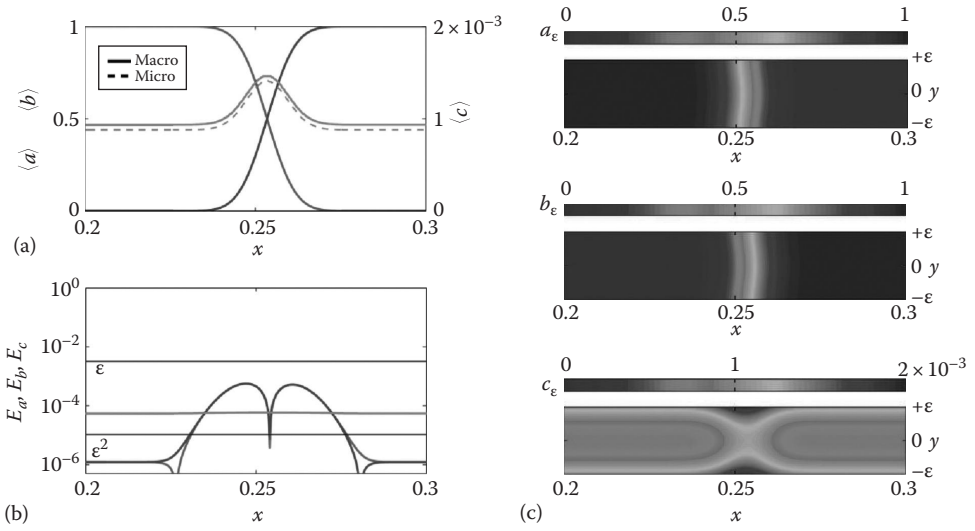

FIGURE 12.7 Example 2. Snapshot of $\langle\psi\rangle_M$ (solid lines) and $\langle\psi\rangle_m$ (dashed lines) with $\psi = \{a,b,c\}$ at time $t = \varepsilon^\alpha$. (a) Longitudinal concentration profiles $\langle\psi\rangle_M$ and $\langle\psi\rangle_m$ obtained from either solving the macroscale system of Equations 12.42 or averaging the pore-scale concentration profiles, respectively. (b) Absolute error along the fracture $E_\psi(x) = |\langle\psi\rangle_m(x) - \langle\psi\rangle_M(x)|$. Horizontal lines identify different orders of magnitude of the absolute error in terms of integer powers of ε. (c) Concentration maps in a portion of the fracture, $x \in [0.2, 0.3]$ and $y = [-\varepsilon, \varepsilon]$, for species A (top), B (middle), and C (bottom) around the original concentration discontinuity $\bar{x} = 0.25$.

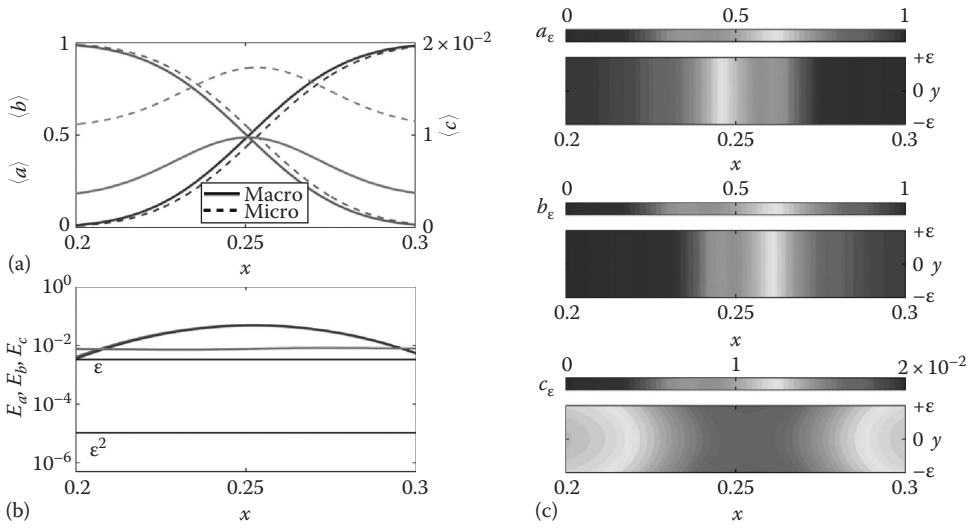

FIGURE 12.8 Example 1. Snapshot of $\langle\psi\rangle_M$ (solid lines) and $\langle\psi\rangle_m$ (dashed lines) with $\psi = \{a,b,c\}$ at time $t = \varepsilon^\alpha$. (a) Longitudinal concentration profiles $\langle\psi\rangle_M$ and $\langle\psi\rangle_m$ obtained from either solving the macroscale system of Equations 12.42 or averaging the pore-scale concentration profiles, respectively. (b) Absolute error along the fracture $E_\psi(x) = |\langle\psi\rangle_m(x) - \langle\psi\rangle_M(x)|$. Horizontal lines identify different orders of magnitude of the absolute error in terms of integer powers of ε. (c) Concentration maps in a portion of the fracture, $x \in [0.2, 0.3]$ and $y = [-\varepsilon, \varepsilon]$, for species A (top), B (middle), and C (bottom) around the original concentration discontinuity $\bar{x} = 0.25$. (Adapted from Boso, F. and Battiato, I., *Adv. Water Resour.*, 62, 254, 2013.)

(see Figure 12.9). Figure 12.9 shows that the adaptivity criteria based on space-time continuum-scale functionals (12.45) and (12.46) provide an accurate (and not too conservative) estimate of where an algorithm refinement is needed, that is, when the errors overcome those predicted by homogenization theory. While alternative criteria could be formulated (e.g., based on macroscopic concentration gradients [82]), the adaptivity criteria (12.45) and (12.46) have the advantage of being *self-consistent* with the upscaling procedure employed to construct the continuum-scale models themselves.

Having criteria to identify subdomains where continuum-scale equations break down, we can proceed by formulating a hybrid model. Before doing that, we review the state-of-art on multiscale methods in the following section.

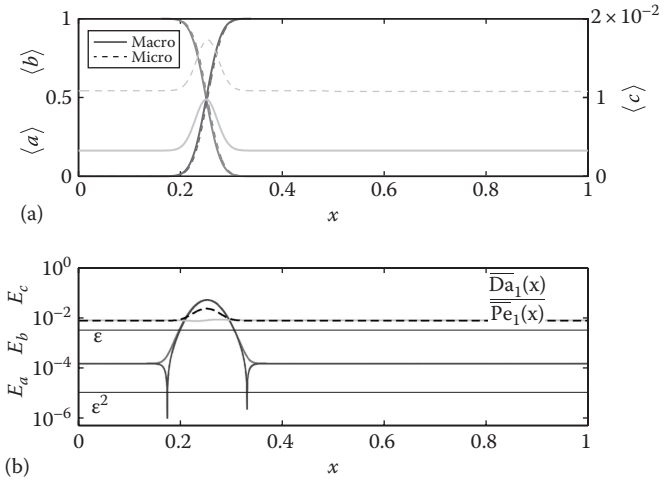

FIGURE 12.9 (a) Snapshots of longitudinal macroscopic concentration $\bar{\psi}$, $\psi = \{a,b,c\}$, of species A, B, and C in a planar fracture with reactive walls, obtained from either solving the continuum-scale equations (solid lines) or averaging the microscale concentration (dashed lines). (b) Absolute error E_ψ along the fracture between continuum- and averaged pore-scale solutions. The adaptive criteria proposed in Equation 12.46 (dashed black line) strongly correlates with E_ψ. (Adapted from Boso, F. and Battiato, I., *Adv. Water Resour.*, 62, 254, 2013.)

12.4 Multiscale and Hybrid Methods

Current deterministic modeling approaches to subsurface flow and transport can be subdivided into pore- and continuum-scale models. While pore-scale models enable one to describe relevant processes with a high degree of fidelity, they are impractical for simulations at scales larger than a small core due to both high computational costs and the lack of detailed information about the pore geometry in the whole computational domain. Despite recent advances in computational methods that allowed fully pore-scale numerical simulations of decimeter-scale samples [86], heterogeneity of most natural porous media and prohibitive computational burden render Lattice Boltzmann modeling, smoothed particle hydrodynamics, and other pore-scale simulations impractical as a predictive tool at the field scale. Continuum models, which treat a porous medium as an "averaged" continuum, overcome these limitations at the cost of relying on phenomenological descriptions. As previously discussed, they fail to predict processes characterized by poor (momentum, mass, heat) mixing at the pore scale, that is, in the presence of high pore-scale gradients. ADE-based models of transport of (bio)chemically reactive solutes can significantly overpredict the extent of reactions in mixing-induced chemical transformations both at the Darcy and field scales [78,87,88, and references therein]. As a result, laboratory-scale measurements of reaction rates in fully-mixed reactors cannot be directly used for field-scale predictions; instead, field-scale model parameters must be calibrated, which raises questions about their applicability for prediction under conditions other than those for which the calibration was performed.

Leading experts in the field of multiscale mathematics and simulation have recently pointed out the need for a unified framework for multiscale simulation that can provide guidelines regarding how to utilize various multiscale simulation approaches [89]. To the best of our knowledge, the multiscale analysis platform proposed by Scheibe et al. [90] represents one of the first organic attempts in that direction (see also [91]) and emerges as a response to the urging need of practitioners to select the most appropriate hybrid multiscale framework for their specific application. The classification scheme is presented in terms of a flow chart with different motifs of hybrid multiscale simulation of flow and transport in the subsurface. Yet, the critical point in the flow chart is the identification of the "degree of coupling" (Question 2, [90]) between fine- and coarse-scale models (e.g., pore and Darcy, or Darcy and field scale). While many authors have recognized the limiting assumptions underlying continuum-scale models [20,75,81,92–94], no general means of quantifying the degree of coupling exists. In the previous sections, we have showed how upscaling of dimensionless fine-scale equations can serve for this purpose, as it allows one to relate the *accuracy* of continuum representations of fine-scale processes with the order of magnitude of relevant dimensionless numbers, which control the time scales of basic transport phenomena (e.g., diffusion, dispersion, advection, reaction). The use of such criteria to adaptively diagnose where, and when, an algorithm refinement is needed, provides a *self-consistent* framework (with upscaling techniques) for top-down model deployment.

The search for ways to combine the physical rigor of pore-scale modeling with the computational efficiency of its continuum-scale counterpart and to model phenomena where the small-scale processes significantly affect large-scale behavior (e.g., material deposition, fracture dynamics) has motivated the development of hybrid pore-scale/continuum-scale algorithms, for example, [95,96], and multiscale approaches, for example, [89,97–103].

It is important to distinguish hybrid algorithms from multiscale numerical approaches that are based on empirical closures [100], upscaling methods [97] and/or assumed macroscopic behavior of microscopic variables [104]. Multiscale algorithms employ "effective" representations of pore-scale processes, which share many approximations and assumptions with continuum models. For example, they employ pore-scale simulations to improve the estimate of continuum-scale effective parameters. On the other hand, hybrid algorithms assume a local breakdown of continuum-scale representations and, consequently cannot rely on any of the assumptions on which the latter are based in order to formulate the coupling between the two scales.

When a global breakdown occurs, alternative modeling techniques for non-Fickian transport should be employed instead. A recent and comprehensive review, discussing nonlocal models such as continuum time random walks [7,105], fractional derivatives [106], and memory function [21,107] approaches, is given in [23].

Hybrid models provide significant computational speed-up when the subdomain Ω_p wherein pore-scale simulations

are required (i.e., wherein continuum models become invalid) is much smaller than the total computational domain Ω. The inequality [108,109],

$$\frac{\|\Omega_{pc}\|}{\|\Omega\|-\|\Omega_p\|}\frac{C_{pc}}{C_p}\ll 1,$$

provides a more precise formulation of this statement. Here $||\Omega||$, $||\Omega_p||$, and $||\Omega_{pc}||$ are the volumes of Ω, Ω_p, and the "handshake" region Ω_{pc} wherein both continuum and pore-scale simulations are coupled, respectively, and C_p and C_{pc} are the computational costs per unit volume for pore-scale and coupling simulations, respectively. This condition takes advantage of the fact that the computational cost of continuum-scale simulations is much smaller than that of pore-scale simulations. As pointed out in [108], a hybrid algorithm is beneficent "even if the algorithmic interface is computationally more expensive than either algorithm, as long as the interface region and the region using the more expensive method are each small fractions of the total volume." The latter condition is satisfied in highly localized flow and transport phenomena, such as flow and transport to/from point sources, and propagation of reactive fronts. Tools for identifying the regions wherein continuum models break down, Ω_p, are developed in Section 12.3.2.

Various methods have been developed to attack these types of scenarios in the context of subsurface hydrology and transport processes. To our best knowledge, the first algorithm refinement method for diffusive systems has been proposed by [108,110], where a hybrid particle/continuum algorithm is formulated for Fickian diffusion and the problem of noise propagation in hybrid simulations is addressed. The particles are taken as independent random walkers and the fluctuating diffusion equation is solved by finite differences with deterministic and white-noise fluxes. Similarly, hybrids for reaction–diffusion systems couple molecular dynamics (MD) and kinetic Monte Carlo simulations, MD and reaction–diffusion equation, and Lattice Boltzmann and reaction–diffusion equation, that is, [95,111,112]. Smoothed particle hydrodynamics (SPH) was used to incorporate moving boundary effects due to precipitation processes at the pore scale [96]. An advantage of SPH over MD lies in requiring a significantly smaller number of particles (and consequently smaller computational costs) to properly model the hydrodynamics of a continuum fluid: this derives from the mesoscopic nature of SPH particles: They are in fact, a collection of MD particles. However, if the Lagrangian particle nature of SPH allows physical and chemical effects to be incorporated into the modeling of flow processes with relatively little code-development efforts, additional complications might arise in the formulation of the coupling boundary conditions in the presence of advection: each particle (both at the pore and continuum scale) moves in space with its own velocity (Stokes or Darcy) and coupling based on superposition of particle spheres of influence becomes unclear. To overcome this complication, [113] proposed an Eulerian hybrid framework. Such a hybrid formulation is *intrusive* (*embedded*) since the upscaled equation has to be modified to incorporate pore-scale effects [113]. The presence of an overlapping region in embedded hybrids requires one to modify existing numerical codes used to conduct both pore- and continuum-scale simulations. Since compatibility with existing codes is a desirable feature of hybrid algorithms, [114,115] have developed *nonintrusive hybrids* in which the overlapping (handshake) region is eliminated. This is accomplished by formulating appropriate conditions at the interfaces separating the two computational subdomains, while ensuring the continuity of state variables and fluxes. Within this framework, fine-scale simulations affect a continuum-scale solution through boundary conditions only. While the nonintrusive formulation requires a larger pore-scale domain compared to that needed by embedded hybridization, the former allows one to take advantage of mismatching grids between the pore- and continuum-scale domains.

Mortar methods (and their subsequent generalizations) allow one to account for multiphysics dynamics within a single macroscopic domain where continuity of fluxes and state variables is enforced between adjacent subdomains through an iterative procedure [116–118]. Application of mortars for hybrid multiscale simulation of subsurface processes has been pioneered by [119–122] and consist in coupling pore-scale network models with macroscopic models. Yet, the employment of pore-scale network models assumes that the system is well mixed at the pore scale. This may not be an accurate assumption especially across sharp reacting fronts whose width can span only few tens of grains [80]. To address this issue, new capabilities in mortar coupling have been recently developed [123], which by an ad hoc procedure allow one to account for different subpore-scale mixing scenarios. The first implementation of mortar approaches that did not employ any parametrization of subpore-scale mixing was implemented for a bioreactive–diffusive system [124] where Darcy-scale equations were directly coupled to fully pore-scale models.

It is worth emphasizing that multiscale and hybrid algorithms share a similar motivating ground, their implementation is inextricably intertwined with the numerical discretization scheme employed in any specific approach and method, so that a unifying organic representation/description of coupling conditions or convergence schemes is unfeasible. Often times, in fact, the coupling is purely numerical with limited physical insight.

For the purpose of demonstration only, we will focus on one approach that can be used to determine coupling conditions when a continuum-scale model fails locally. In the following, we will focus on coupling formulations that, based on upscaling methods (e.g., volume averaging), retain a strong physics flavor. In particular, we will focus on two coupling schemes: embedded (Section 12.4.1) and nonintrusive (Section 12.4.2) with or without overlapping between the pore- and the continuum-scale domains, respectively. Finally, we will conclude with a case study (Section 12.4.3). We think this represents a natural conclusion to a chapter devoted to the theory and numerics of multiscale dynamics.

Otherwise, we refer to [90] for a thorough review of multiscale and hybrid approaches in subsurface hydrology, with a rich list of technical references for the interested reader.

12.4.1 Embedded Schemes

To set the basic ideas of hybrid modeling, we consider advective-diffusive transport in a fully saturated porous medium Ω^T. Within the pore space $\Omega^T_{\text{pore}} \subset \Omega^T$, single-phase flow of an incompressible fluid is described by the Stokes and continuity equations. Flow equations are subject to the no-slip boundary condition on the solid–liquid interface $\mathcal{A}_{\ell s}$, which is taken to be impermeable to flow. The flow is driven by boundary conditions imposed on $\partial\Omega^T$, the external boundary of Ω^T. The fluid contains a dissolved species with molar concentration $c(\mathbf{x}, t)$ that is advected and diffused in Ω^T_{pore}. The evolution of the concentration $c(\mathbf{x}, t)$ of a tracer undergoing advection and diffusion is described by

$$\frac{\partial c}{\partial t} + \nabla \cdot (\mathbf{v}c) = \mathcal{D}\nabla^2 c, \tag{12.47}$$

subject to a flux boundary condition on the solid–fluid interface $A_{\ell s}$

$$-\mathbf{n} \cdot \mathcal{D}\nabla c = \mathcal{K}c, \tag{12.48}$$

and proper boundary conditions on $\partial\Omega^T$.

We focus on transport regimes in which the validity of the continuum-scale transport equation (12.50) breaks down in a subdomain $\Omega_p \subset \Omega^T_{\text{pore}}$ (with boundary $\partial\Omega_p$) of the computational domain (see Figure 12.10). Under such transport conditions, the spatial averaging of Equation 12.47 in Ω_p yields an integro-differential equation [113]

$$\phi \frac{\partial \langle c \rangle}{\partial t} = \langle \nabla \cdot (\mathcal{D}\nabla c - \mathbf{v}c) \rangle \tag{12.49}$$

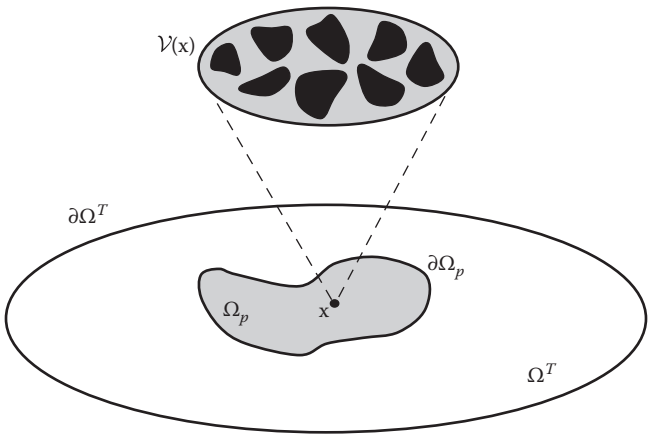

FIGURE 12.10 A schematic representation of the pore- and continuum-scale domains and the averaging procedure leading to *intrusive* (embedded) hybridization: the subdomain where continuum-scale representation breaks down is depicted in gray; its boundary is $\partial\Omega_p$.

rather than a standard advection-dispersion equation

$$\phi \frac{\partial \langle c \rangle}{\partial t} + \phi \nabla \cdot (\langle \mathbf{v} \rangle \langle c \rangle) = \nabla \cdot (\mathbf{D}^\star \nabla \langle c \rangle) - \mathcal{K}^\star \langle c \rangle, \tag{12.50}$$

where $\langle \mathbf{v} \rangle$ is the average macroscopic velocity, $\mathbf{D}^\star$ is the dispersion coefficient, and $\mathcal{K}^\star$ is the effective reaction rate. Violation of some of the sufficient conditions for applicability of macroscale models identified in Section 12.3 [82,83] prevents the averaging integrals in Equation 12.49 from being converted into the corresponding terms for the macroscopic (average) concentration $\langle c \rangle$ in Equation 12.50. The averaging in Equation 12.49 is defined over $\mathcal{V}(\mathbf{x}^*) \equiv \Omega_p(\mathbf{x}^*)$ and $\mathbf{x}^*$ is the centroid of Ω_p, that is, the subdomain Ω_p shrinks to a point $\mathbf{x}^* \in \Omega^T$ (see Figure 12.10). Similarly, the averaging in Equation 12.50 is defined over $\mathcal{V}(\mathbf{x})$ with $\mathbf{x} \in \Omega^T$ and $\mathbf{x} \neq \mathbf{x}^*$. According to Gauss' theorem, Equation 12.49 can be written as

$$\phi \frac{\partial \langle c \rangle}{\partial t} = -\frac{1}{\phi |\Omega_p|} \int_{\Gamma_{\ell\ell}} q_n \, \mathrm{d}s - \frac{1}{\phi |\Omega_p|} \int_{\Gamma_{s\ell}} \mathcal{K}c \, \mathrm{d}s, \tag{12.51}$$

where $\Gamma_p = \Gamma_{\ell\ell} \cup \Gamma_{s\ell}$ is the bounding surface of Ω_p consisting of liquid–liquid ($\Gamma_{\ell\ell}$) and solid–liquid ($\Gamma_{s\ell}$) segments and $\mathrm{d}s$ is an infinitesimal element of Γ_p. Also, $q_n = \mathbf{n} \cdot (-\mathcal{D}\nabla c + \mathbf{v}c)$ is the *unknown* pore-scale mass flux (or flux density) through the liquid–liquid portion of the boundary Γ_p. The RHS of Equation 12.51 depends on pore-scale quantities and represents the coupling term between pore and continuum scale. Such a hybrid formulation is *intrusive* (*embedded*) since the RHS of Equation 12.49 has to be modified to incorporate pore-scale effects as indicated in Equation 12.51 when $\mathbf{x} = \mathbf{x}^\star$, that is, the full pore-scale problem (12.47) must be solved in $\Omega_p(\mathbf{x}^\star)$. For $\mathbf{x} \neq \mathbf{x}^\star$, the standard macroscale equation (12.50) can be employed instead.

In summary, the hybrid pore-scale/continuum-scale algorithm contains the three unknowns (c, $\langle c \rangle$, q_n) that satisfy a system of coupled partial-differential equations,

$$\phi \frac{\partial \langle c \rangle}{\partial t} + \phi \nabla \cdot (\langle \mathbf{v} \rangle \langle c \rangle) = \nabla \cdot (\mathbf{D}^\star \nabla \langle c \rangle) - \mathcal{K}^\star \langle c \rangle,$$
$$\mathbf{x} \in \Omega^T, \quad \mathbf{x} \neq \mathbf{x}^\star, \quad t > 0, \tag{12.52}$$

$$\phi \frac{\mathrm{d}\langle c \rangle}{\mathrm{d}t} = \frac{1}{\phi |\Omega_p|} \int_{\Gamma_{\ell\ell}} q_n \, \mathrm{d}\mathbf{x} - \frac{1}{\phi |\Omega_p|} \int_{\Gamma_{s\ell}} \mathcal{K}c \, \mathrm{d}\mathbf{x}, \quad \mathbf{x} = \mathbf{x}^\star, \quad t > 0, \tag{12.53}$$

$$\frac{\partial c}{\partial t} + \nabla \cdot (\mathbf{v}c) = \mathcal{D}\nabla^2 c, \quad \mathbf{x} \in \Omega_p(\mathbf{x}^\star), \quad t > 0, \tag{12.54}$$

$$\mathbf{n} \cdot (\mathcal{D}\nabla c - \mathbf{v}c) = q_n, \quad \mathbf{x} \in \Gamma_{\ell\ell}, \quad t > 0, \tag{12.55}$$

$$-\mathbf{n}\cdot\mathcal{D}\nabla c = \mathcal{K}c, \quad \mathbf{x}\in\Gamma_{s\ell}, \quad t>0, \tag{12.56}$$

supplemented by boundary conditions on the external domain $\partial\Omega^T$ and initial conditions. The former system of equations can be solved using an iterative procedure as sketched in Figure 12.11. We emphasize that Equations 12.53 and 12.54 are solved at the continuum and pore scales in overlapping domains as showed in Figure 12.11. The iteration starts by guessing the value of the unknown flux q_p (Step 1). This allows one to solve the pore-scale problem in Ω_p, Equations 12.54 through 12.56, and determine the RHS of Equation 12.53 (Step 2). Then Equations 12.52 and 12.53 can be solved for the continuum-scale concentration and the fluxes at the boundary calculated from numerical differentiation and can be compared with the initial guess (Step 3). The initial guess is then refined until convergence is achieved.

The presence of an overlapping region in embedded hybrids requires one to modify existing numerical codes used to conduct both pore- and continuum-scale simulations. Even though this intrusive formulation is general and can be applied to a variety of different numerical schemes, its implementation in legacy codes, in which discretized equations cannot be easily modified by the user, is challenging.

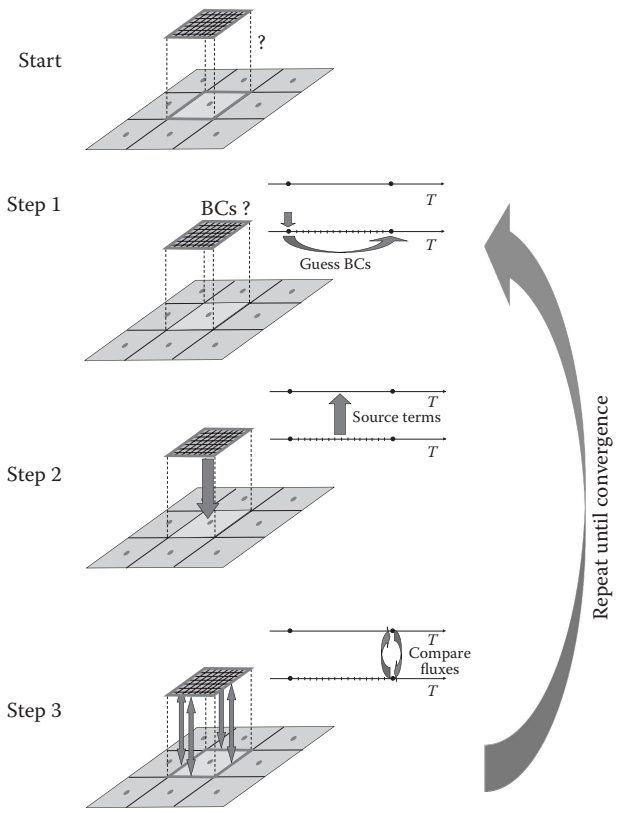

FIGURE 12.11 Steps of a hybrid algorithm. Step 1: The iteration starts by guessing the value of the unknown flux q_n on the boundary shared by the pore-scale and continuum-scale domains. Step 2: This initial guess allows one to solve the pore-scale problem in Ω_p, Equations 12.54 through 12.56, and determine the RHS of Equation 12.53. Step 3: Equations 12.52 and 12.53 can be solved for the continuum-scale concentration and the fluxes at the boundary calculated from numerical differentiation and can be compared with the initial guess. The initial guess is then refined until convergence is achieved.

12.4.2 Nonintrusive Schemes

A desirable feature of a hybrid algorithm is its portability and implementation in existing codes. This can be accomplished by eliminating the overlapping ("handshake") region and formulating appropriate conditions at the interfaces separating the two computational subdomains, while ensuring the continuity of state variables and fluxes. Within this framework, pore-scale simulations affect a continuum-scale solution through boundary conditions (and not as a modification of continuum-scale discretized equations): this will facilitate hybrid implementation for existing codes and/or software.

12.4.2.1 Derivation of Coupling Boundary Conditions

Again, we are concerned with transport regimes in which the validity of the continuum-scale transport equation (12.50) breaks down in a subdomain $\Omega_p \subset \Omega^T_{pore}$ with boundary $\partial\Omega_p$ of the computational domain Ω. We define Γ to be the locus of the centers of the family of the averaging volumes $\mathcal{V}(\mathbf{x})$, whose envelope is $\partial\Omega_p$ as shown in Figure 12.12. We denote $\bar{\Omega}_p$ the domain bounded by Γ. Let $\mathcal{A}_{s\ell} = \bar{\Omega}_p \cap \mathcal{A}^T_{s\ell}$.

Let $\langle c\rangle^{\leftarrow}$ denote the limiting value of $\langle c\rangle(\mathbf{x})$ as $\mathbf{x}\to\mathbf{x}^{\leftarrow}\in\Gamma$ from the *exterior* of $\bar{\Omega}_p$, and $\langle c\rangle^{\rightarrow} = \langle c\rangle(\mathbf{x}^{\rightarrow})$ as $\mathbf{x}\to\mathbf{x}^{\rightarrow}\in\Gamma$ from the *interior* of $\bar{\Omega}_p$, where the averages are defined over the supports $\mathcal{V}(\mathbf{x}^{\leftarrow})$ and $\mathcal{V}(\mathbf{x}^{\rightarrow})$, respectively. Since average concentration is a continuous function everywhere in Ω, it is continuous across Γ [114]

$$\langle c\rangle^{\leftarrow} = \langle c\rangle^{\rightarrow} \quad \text{for}\,|\,\mathbf{x}^{\rightarrow}-\mathbf{x}^{\leftarrow}\,|\to 0. \tag{12.57}$$

Let $\mathcal{V}^{in}(\mathbf{x}) := \mathcal{V}(\mathbf{x})\cap\bar{\Omega}_p$ and $\mathcal{V}^{out}(\mathbf{x}) := \mathcal{V}(\mathbf{x})\backslash\mathcal{V}^{in}(\mathbf{x})$ to form a partition of $\mathcal{V}$ where pore scale is explicitly resolved and where only a continuum-scale representation exists, respectively (see Figure 12.12). Then Equation 12.57 can be written as

$$\langle c\rangle^{\leftarrow} = \frac{1}{\phi\|\mathcal{V}\|}\int_{\mathcal{V}^{in}(\mathbf{x}^{\rightarrow})} c(\mathbf{y})\,d\mathbf{y} + \frac{1}{\phi\|\mathcal{V}\|}\int_{\mathcal{V}^{out}(\mathbf{x}^{\rightarrow})} c(\mathbf{y})\,d\mathbf{y}\,. \tag{12.58}$$

Expanding $c(\mathbf{y})$ into a Taylor series around the centroid $\mathbf{x}$ and retaining the leading term yields

$$\int_{\mathcal{V}^{out}(\mathbf{x}^{\rightarrow})} c\,d\mathbf{y} \approx \left\|\mathcal{V}^{out}(\mathbf{x}^{\rightarrow})\right\| c^{\rightarrow}(\mathbf{x}^{\rightarrow}). \tag{12.59}$$

Inserting Equation 12.59 into Equation 12.58, one obtains

$$\bar{c}^{\leftarrow} = \frac{1}{\phi\|\mathcal{V}\|}\int_{\mathcal{V}^{in}(\mathbf{x}^{\rightarrow})} c(\mathbf{y})\,d\mathbf{y} + \frac{\left\|\mathcal{V}^{out}(\mathbf{x}^{\rightarrow})\right\|}{\phi\|\mathcal{V}\|} c^{\rightarrow}\,. \tag{12.60}$$

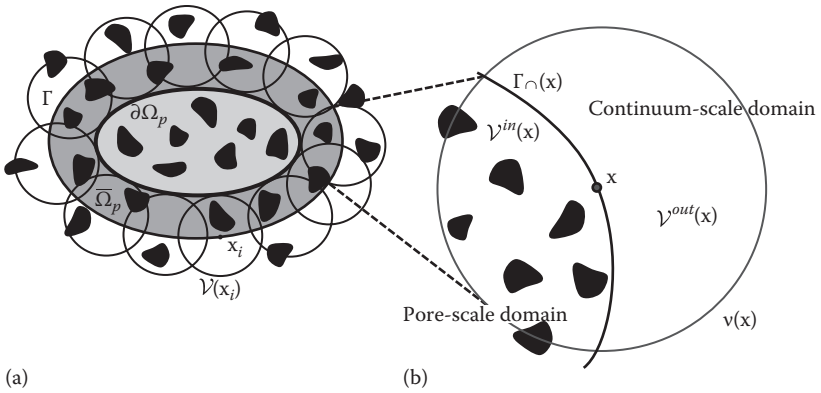

FIGURE 12.12 (a) The subdomain where continuum-scale representation breaks down is depicted in gray. Its boundary is $\partial\Omega_p$. In the *nonintrusive* hybrid formulation, the boundary Γ is constructed as the locus of the centers of the family of averaging volumes $\mathcal{V}(\mathbf{x})$ whose envelope is $\partial\Omega_p$. The red indicates the additional pore-scale domain necessary to define the *nonintrusive* boundary conditions. (b) A schematic representation of the averaging procedure across the boundary separating pore-scale and continuum-scale representations. On the left of Γ the pore-scale is fully resolved while on the right of Γ only a continuum-scale representation exists. (Adapted from Youzefzadeh, M. and Battiato, I., *Water Resour. Res.*, submitted, 2016.)

Following a similar procedure, a flux continuity condition is expressed as [114]

$$\mathbf{n}\cdot(-\mathbf{D}^{*}\nabla\langle c\rangle^{\leftarrow}+\phi\langle\mathbf{v}\rangle\langle\overline{c}\rangle^{\leftarrow})=\frac{1}{|\mathcal{V}|}\mathbf{n}\cdot\int_{\mathcal{V}^{in}(\mathbf{x}^{\rightarrow})}(-\mathcal{D}\nabla c+\mathbf{v}c)\,\mathrm{d}\mathbf{y}+q_n\,, \tag{12.61}$$

where

$$q_n(\mathbf{x}):=\frac{1}{|\mathcal{V}|}\mathbf{n}\cdot\int_{\mathcal{V}^{out}(\mathbf{x})}(-\mathcal{D}\nabla c+\mathbf{v}c)\mathrm{d}\mathbf{y} \tag{12.62}$$

is an unknown flux through Γ. This flux serves as a coupling condition at the interface between pore- and continuum-scale subdomains.

The final form of the coupled system of equations for the nonintrusive hybrid algorithm is

$$\phi\frac{\partial\langle c\rangle}{\partial t}+\phi\nabla\cdot(\langle\mathbf{v}\rangle\langle c\rangle)=\nabla\cdot(\mathbf{D}^{*}\nabla\langle c\rangle)-\mathcal{K}^{*}\langle c\rangle,\quad \mathbf{x}\in\Omega\setminus\bar{\Omega}_p, \tag{12.63}$$

$$\frac{\partial c}{\partial t}+\nabla\cdot(\mathbf{v}c)=\mathcal{D}\nabla^{2}c,\quad \mathbf{x}\in\bar{\Omega}_p, \tag{12.64}$$

$$-\mathbf{n}\cdot\mathcal{D}\nabla c=\mathcal{K}c,\quad \mathbf{x}\in\mathcal{A}_{s\ell}, \tag{12.65}$$

$$\mathbf{n}\cdot(-\mathcal{D}\nabla c+\mathbf{v}c)=q_n,\quad \mathbf{x}\in\Gamma, \tag{12.66}$$

$$\langle c\rangle^{\leftarrow}=\frac{1}{\phi|\mathcal{V}|}\int_{\mathcal{V}^{in}(\mathbf{x})}c\,\mathrm{d}\mathbf{y}+\frac{|\mathcal{V}^{out}|}{\phi|\mathcal{V}|}c^{\rightarrow},\quad \mathbf{x}\in\Gamma, \tag{12.67}$$

$$\mathbf{n}\cdot(\mathbf{D}^{*}\nabla\langle c\rangle^{\leftarrow}-\phi\mathcal{V}\langle c\rangle^{\leftarrow})=q_n+\frac{1}{|\mathcal{V}|}\mathbf{n}\cdot\int_{\mathcal{V}^{in}(\mathbf{x}^{\rightarrow})}(-\mathcal{D}\nabla c+\mathbf{v}c)\mathbf{d}\mathbf{y},\quad \mathbf{x}\in\Gamma. \tag{12.68}$$

The interfacial conditions (12.67) and (12.68) are reminiscent of the macroscopic Dirichlet and Neumann boundary conditions derived by the method of volume averaging in [125]. While similar in spirit, the previous conditions do not require a closure approximation and rely on pore-scale simulations instead.

The solution of the coupled system (12.63) through (12.68) reduces to finding zeros of a system of equations in the form

$$F(q_n,c^{\rightarrow})=0,\quad G(q_n,c^{\rightarrow})=0, \tag{12.69}$$

where

$$F(q_n,c^{\rightarrow})=\mathbf{n}\cdot(\mathbf{D}^{*}\nabla\langle c\rangle^{\leftarrow}-\phi\langle\mathbf{v}\rangle\langle c\rangle^{\leftarrow})-\frac{1}{|\mathcal{V}|}\int_{\mathcal{V}^{in}(\mathbf{x}^{\rightarrow})}\mathbf{n}\cdot(-\mathcal{D}\nabla c+\mathbf{v}c)\mathrm{d}\mathbf{y}-\frac{|\Gamma(\mathbf{x}^{\rightarrow})|}{|\mathcal{V}|}q_n, \tag{12.70}$$

$$G(q_n,c^{\rightarrow})=\langle c\rangle^{\leftarrow}-\frac{1}{\phi|\mathcal{V}|}\int_{\mathcal{V}^{in}(\mathbf{x})}c\,\mathrm{d}\mathbf{y}-\frac{|\mathcal{V}^{out}|}{\phi|\mathcal{V}|}c^{\rightarrow}, \tag{12.71}$$

coupled to Equations 12.63 through 12.66.

The hybrid pore-scale/continuum-scale algorithm can be formulated as a zero-finding algorithm for *F* and *G* through an iterative procedure similar to the one outlined in the previous section. Detailed derivations can be found in [114,115].

12.4.3 Case Study: Taylor Dispersion between Reactive Plates

In order to illustrate the coupling, in this section, we consider transport of a reactive solute by advection and diffusion in a fracture of width $2H$. The solute undergoes a first-order heterogeneous reaction at the walls of the channel. The flow domain $\Omega = \{(x, y): x \in (0, \infty), |y| < H\}$ has the boundary $\Gamma = \{(x, y): x \in (0, \infty), |y| = H\}$.

Assuming laminar, fully developed flow inside the fracture, the "pore-scale" velocity is given by Poiseuille's law, $\mathbf{v} = (u, 0)^{\mathrm{T}}$, where

$$u(y) = u_m\left[1-\left(\frac{y}{H}\right)^2\right] \tag{12.72}$$

and u_m is the maximum velocity at the center of the fracture ($y = 0$). Hence, the pore-scale concentration satisfies

$$\frac{\partial c}{\partial t} + u(y)\frac{\partial c}{\partial x} - \mathcal{D}\left(\frac{\partial^2 c}{\partial x^2} + \frac{\partial^2 c}{\partial y^2}\right) = 0, \quad (x, y) \in \Omega, \quad t > 0, \tag{12.73}$$

$$-\mathcal{D}\frac{\partial c}{\partial y} = \mathcal{K}c, \quad (x, y) \in \Gamma, \quad t > 0. \tag{12.74}$$

The average concentration $\langle c\rangle(x, t)$ is now defined as

$$\langle c\rangle(x, t) \equiv \frac{1}{2H}\int_{-H}^{H} c(x, y, t)\mathrm{d}y. \tag{12.75}$$

Upscaling of Equations 12.73 and 12.74 via homogenization technique gives [43]

$$\frac{\partial\langle c\rangle}{\partial t} + U\frac{\partial\langle c\rangle}{\partial c} + \mathcal{K}^\star\langle c\rangle = D^\star\frac{\partial^2\langle c\rangle}{\partial x^2}, \quad x \in (0, \infty), \quad t > 0, \tag{12.76}$$

where

$$U = u_m\left(\frac{2}{3} + \frac{4\mathrm{Da}_y}{45}\right), \quad \mathcal{K}^\star = \frac{\mathcal{K}}{H}\left(1 - \frac{\mathrm{Da}_y}{3}\right), \quad D^\star = \mathcal{D}\left(1 + \frac{8\mathrm{Pe}_y^2}{945}\right), \tag{12.77}$$

and

$$\mathrm{Pe}_y = \frac{u_m H}{\mathcal{D}}, \quad \mathrm{Da}_y = \frac{\mathcal{K}H}{\mathcal{D}}. \tag{12.78}$$

The validity of Equations 12.76 through 12.78 requires that L, a macroscopic characteristic length scale in the x direction, be much larger than H, that is, $\varepsilon = H/L \ll 1$, and places a number of constraints on the order of magnitude of Pe_y and Da_y. In particular, $\mathrm{Da}_y < 3$ as evidenced by Equation 12.77 where $\mathcal{K}^\star$ changes sign if $\mathrm{Da}_y > 3$.

In order to test the hybrid coupling performance, transport in a chemically heterogeneous fracture is considered with initial pore-scale concentration $c(x, y, 0) = 1$ and boundary conditions of constant injection, $c(0, y, t) = 0$, and zero flux at the inlet and outlet, respectively. Specifically, a finite portion of the fracture is four orders of magnitude more reactive then the rest (see Figure 12.13a), such that the typical Damköhler number ranges from 6.25×10^{-4} to 2.56. Equations 12.76 through 12.78 fails for $\mathrm{Da}_y \geq 3$ as the effective reaction coefficient $\mathcal{K}^\star$ changes sign for increasing positive values of $\mathcal{K}$ (i.e., increasing mass loss at the solid–liquid interface): this leads to the unphysical behavior of $\mathcal{K}^\star < 0$ (i.e., source) while mass is absorbed (degraded) at the microscale (i.e., sink). While it is clear that differences between the upscaled model, (12.76) through (12.78), and a fully 2D pore-scale solution will be dramatic for $\mathrm{Da}_y \geq 3$, we show here that significant deviations from the "pore-scale" solution occur even for $\mathrm{Da}_y < 3$. This is done by comparing the results of hybrid (embedded and nonintrusive, Figure 12.13b and c, respectively) simulations with that of the upscaled 1D equation (Figure 12.13d) and the average of the fully 2D solution (Figure 12.13a).

Figures 12.14 [113] and 12.15a [114] compare the continuum-scale concentration obtained from the upscaled 1D continuum-scale, hybrid, and fully 2D pore-scale equations, for both the embedded and nonintrusive schemes, respectively. At the location of high heterogeneity, the continuum-scale equation overestimates the concentration, with values that double the true

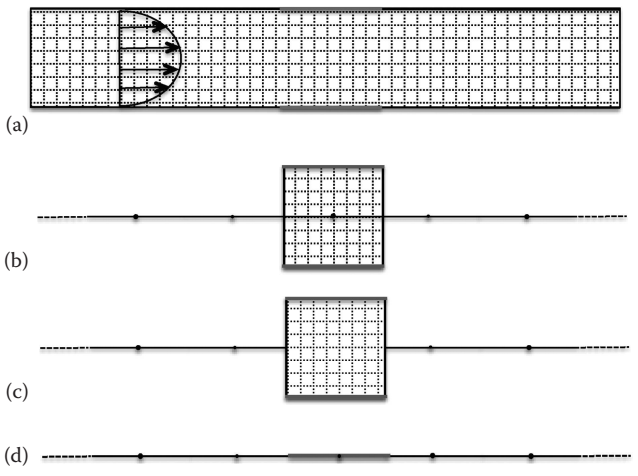

FIGURE 12.13 (a) Two-dimensional fracture with chemically heterogeneous reactive walls. The orange portion represents the location where the wall reactivity is much higher than its surroundings. (b) Representation of an embedded hybrid coupling where the pore-scale (2D) domain overlaps with the continuum-scale (1D) domain. (c) Sketch of an nonintrusive hybrid coupling where the continuum- and pore-scale domains have no overlapping region and the coupling is performed exclusively through boundary conditions. (d) Upscaled macroscopic 1D fracture model.

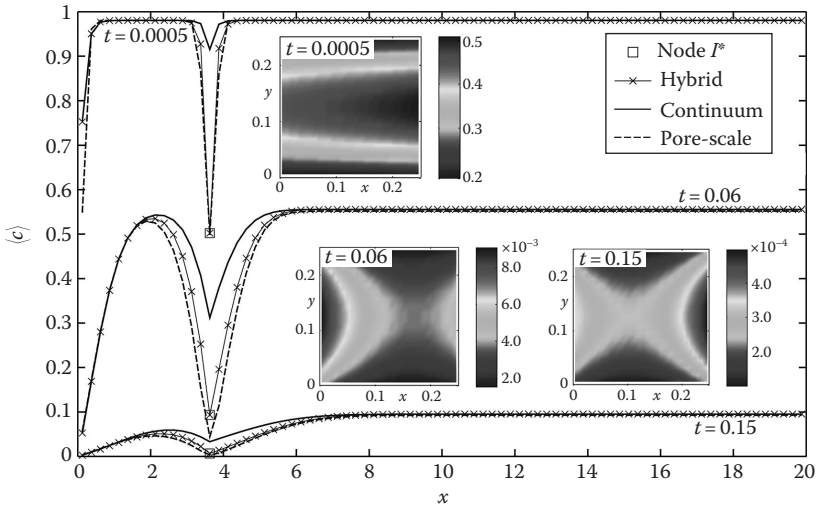

FIGURE 12.14 Temporal snapshots of the average concentration $\langle c \rangle(x, t)$ computed with the 1D continuum model (solid line), *embedded* hybrid algorithm (×) and fully resolved 2D pore-scale simulations (dashed line) at three different instances in time. Symbol □ indicates the location where the pore and continuum scales are coupled. Insets: pore-scale concentration $c(x, y, t)$ at the fully resolved node for three different times. (Adapted from Battiato, I. et al., *Adv. Water Resour.*, 34(9), 1140, 2011.)

concentration obtained from the pore-scale simulations. On the contrary, both hybrid schemes significantly improve the predictions. The insets in Figure 12.14 depict the concentration profile at the pore scale at three different times and shows how the highly reacting walls produce strong concentration gradients between areas where mass is more quickly depleted because of fast reactions (close to the walls) relative to others where the major transport mechanism is diffusion (in the center of the channel). Importantly, Figure 12.15 (bottom) plots the absolute error of the nonintrusive (thin dashed line) and continuum (thin solid line) models relative to the fully 2D pore-scale solution. The error in the hybrid simulation is bounded by ε^2 as predicted by homogenization technique. This suggests that if proper coupling conditions are established when local breakdown of macroscopic equations occurs, then model predictivity, that is, rigorous modeling error bounds, can be preserved.

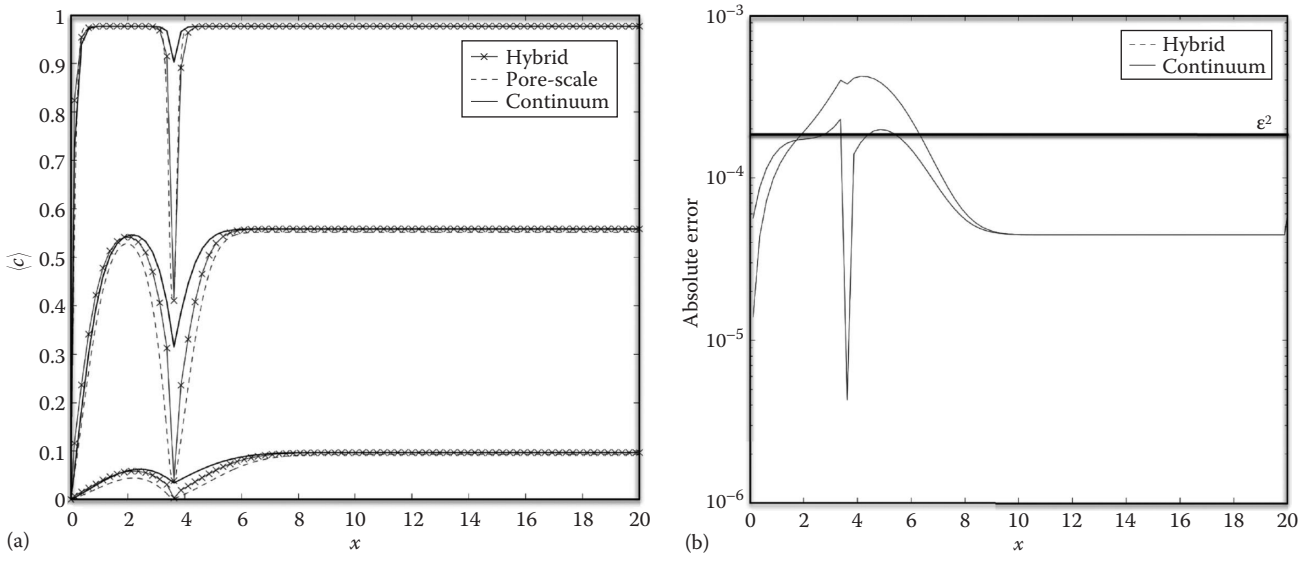

FIGURE 12.15 (a) Temporal snapshots of the average concentration $\langle c \rangle(x, t)$ computed with the 1D continuum model (solid line), *nonintrusive* hybrid algorithm (×) and fully-resolved 2D pore-scale simulations (dashed line) at times $t = 0.0005$ (top), $t = 0.015$ (center) and $t = 0.06$ (bottom). (b) Absolute error in the 1D and hybrid simulations and error bound prescribed by homogenization theory (horizontal line). (Adapted from Youzefzadeh, M. and Battiato, I., *Water Resour. Res.*, submitted, 2016.)

12.5 Conclusions and Outlook

Modeling flow and reactive transport in the subsurface is an extremely challenging task due to the presence of heterogeneity on a continuity of scales, nonlinear processes, and partial or total lack of scale separation. These problems have continued challenging modelers for decades. While much progress has been recently made to construct seamless models of "fully resolved" pore-scale domains as large as lab cores, there is an uphill and long path toward a fully integrated multiscale framework (Figure 12.2) able to accurately model process dynamics *across* relevant spatial and temporal scale (i.e., up to the field or reach scale), while accounting for accurate across-scale coupling.

The development of multiscale and hybrid algorithms that explicitly account for across-scale coupling gives rise to a set of new challenges. Tackling the latter is critical if multiscale modeling capabilities are to transition from theory to practice. In the following, we provide an incomplete list of future challenges that will need to be addressed in the context of hybrid simulators and multiscale algorithms at large.

- Most subsurface hydrology applications call for ultralong time (hundreds or thousands of years) predictions of subsurface system response to unsteady, and potentially highly fluctuating, forcing factors, that is, for temporally-upscaled continuum-scale models of time-averages, $\{\psi\}(\mathbf{x}, t) := (2\Delta T)^{-1}\int_{t-\Delta T}^{t+\Delta T} \psi(\mathbf{x}, t')\mathrm{d}t'$, where $2\Delta T$ is the time-averaging window, or time support representative volume, and ψ is a fine- or coarse-scale spatially averaged quantity. Yet, while standard in the theory of turbulence [126], the time-averaging of fine-scale models of flow in porous media and geologic formations [64,127] have attracted, to the best of our knowledge, much less attention compared to its overbearing spatial-averaging sibling. The importance of temporal resolution of time-fluctuating boundary conditions and forcing factors in highly nonlinear systems has been demonstrated for nonlinear transport in the vadose zone where macroscale model predictions are greatly affected by the time resolution of forcing factors (e.g., annual versus hourly meteorological data) [128]. A systematic approach to handle slow (seasonal) and fast (daily) temporal fluctuations of, for example, boundary conditions (e.g., momentum and mass fluxes) is critical to understand and predict system resilience under global climate changes.
- The understanding of uncertainty propagation across scales in hybrid/multiscale models is still at its infancy, despite few recent advancements [110,129]. For example, the impact of unknown pore-scale geometry on multiscale algorithms needs to be studied and quantified in order to provide robust quantification of uncertainty in multiscale model predictions.
- Similarly, parametric uncertainty in multiscale models must be accounted for. While Monte Carlo simulations appear unrealistic in a multiscale framework, stochastic multiscale approaches could be a viable option to handle both aleatoric and epistemic uncertainties.
- Data assimilation will be critical to reduce uncertainty in multiscale models. New multiscale data assimilation techniques should be designed that are best suited for multiscale models.

While the path ahead is challenging, it seems appropriate to conclude this chapter on Albert Einstein's note that "everything should be made as simple as possible but not simpler."

Acknowledgments

Partial support from EAR NSF under award "Collaborative Research: Hybrid Modeling of Reactive Transport in Porous and Fractured Media" and Battelle Memorial Institute grant "Hydro-Biogeochemical Process dynamics in the Groundwater Surface Water Interaction Zone" is gratefully acknowledged.

References

1. NSF, *Simulation-Based Engineering Science: Revolutionizing Engineering Science through Simulation*, National Science Foundation Blue Ribbon Panel on Simulation-Based Science, Washington, DC (2006).
2. D. M. Tartakovsky, Assessment and management of risk in subsurface hydrology: A review and perspective, *Adv. Water Resour.* **51**, 247–260 (2013).
3. J. Gomez-Hernandez, Complexity, *Ground Water* **44**(6), 782–785 (2006).
4. M. Hill, The practical use of simplicity in developing ground water models, *Ground Water* **44**(6), 775–781 (2006).
5. BERAC, Virtual laboratory: Innovative framework for biological and environmental grand challenges, A Report from the Biological and Environmental Research Advisory Committee, DOE/SC-0156 (2013). http://science.energy.gov/~/media/ber/berac/pdf/20130221/BERACVirtualLaboratory_Feb-18-2013.pdf.
6. U.S. Department of Energy, Office of Basic Energy Sciences, Basic Research needs for geosciences: Facilitating 21st century energy systems (2007). http://science.energy.gov/~/media/bes/pdf/reports/files/geo_rpt.pdf.
7. J. H. Cushman, On unifying the concepts of scale, instrumentation, and stochastics in the development of multiphase transport theory, *Water Resour. Res.* **1668–1676**, 20 (1984).
8. J. H. Cushman, On measurement, scale, and scaling, *Water Resour. Res.* **22**(2), 129–134 (1986).
9. J. H. Cushman, *Dynamics of Fluids in Hierarchical Porous Media*. Academic Press, San Diego, CA (1990).
10. J. H. Cushman, *The Physics of Fluids in Hierarchical Porous Media: Angstroms to Miles*. Kluwer Academic Publisher, New York (1997).

11. S. C. Jose and O. A. Cirpka, Measurement of mixing-controlled reactive transport in homogeneous porous media and its prediction from conservative tracer test data, *Environ. Sci. Technol*. **38**(7), 2089–2096 (2004).
12. L. Luquot and P. Gouze, Experimental determination of porosity and permeability changes induced by massive injection of CO_2 into carbonate reservoirs, *Chem. Geol*. **265**, 148–159 (2009).
13. C. Geloni, T. Giorgis, and A. Battistelli, Modeling of rocks and cement alteration due to co_2 injection in an exploited gas reservoir, *Transp. Porous Media* **90**, 183–200 (2011).
14. J. Qajar, N. Francois, and C. H. Arns, Micro-tomographic characterization of dissolution-induced local porosity changes including fine migration in carbonate rocks, 153216-MS. *SPE EOR Conference at Oil and Gas West Asia*, Society of Petroleum Engineers, Muscat, Oman (2012).
15. P. O. Mangane, L. Gouze, P. Gouze, and L. Luquot, Permeability impairment of a limestone reservoir triggered by heterogenous dissolution and particle migration during CO_2-righ injection, *Geophys. Res. Lett*. **17**, 4114–4619 (2013).
16. L. Luquot, O. Rodriguez, and P. Gouze, Experimental characterization of porosity structure and transport property changes in limestone undergoing different dissolution regimes, *Transp. Porous Media* **101**, 507–532 (2014).
17. M. M. Smith, Y. Sholokhova, Y. Hao, and S. A. Carroll, Evaporite caprock integrity: An experimental study of reactive mineralogy and pore-scale heterogeneity during brine-CO_2 exposure, *Environ. Sci. Technol*. **47**(1), 262–268 (2012).
18. R. Ma, C. Zheng, C. Liu, J. Greskowiak, H. Prommer, and J. Zachara, Assessment of controlling processes for field-scale uranium reactive transport under highly transient flow conditions, *Water Resour. Res*. **50**, 1006–1024 (2014).
19. J.-H. Lee, J. M. Zachara, J. K. Fredrickson, S. M. Heald, J. P. McKinley, A. E. Plymale, C. T. Resch, and D. A. Moore, Fe(II)- and sulfide-facilitated reduction of $^{99}Tc(VII)O_4^-$ in microbially reduced hyporheic zone sediments, *Geochim. Cosmochim. Acta* **136**, 247–264 (2014).
20. B. D. Wood, The role of scaling laws in upscaling, *Adv. Water Resour*. **32**(5), 723–736 (2009).
21. O. Silva, J. Carrera, M. Dentz, S. Kumar, A. Alcolea, and M. Willmann, A general real-time formulation for multi-rate mass transfer problems, *Hydrol. Earth Syst. Sci*. **13**, 1399–1411 (2009).
22. W. Um, R. J. Serne, S. B. Yabusaki, and A. T. Owen, Enhanced radionuclide immobilization and flow path modifications by dissolution and secondary precipitates, *J. Environ. Qual*. **34**, 1404–1414 (2005).
23. S. P. Neuman and D. M. Tartakovsky, Perspective on theories of anomalous transport in heterogeneous media, *Adv. Water Resour*. **32**(5), 670–680 (2009).
24. S. Whitaker, *The Method of Volume Averaging*. Kluwer Academic Publishers, Dordrecht, the Netherlands (1999).
25. F. Valdes-Parada, J. Ochoa-Tapia, and J. Alvarez-Ramirez, On the effective viscosity for the Darcy-Brinkman equation, *Phys. A* **385**, 69–79 (2007).
26. P. E. Kechagia, I. N. Tsimpanogiannis, Y. C. Yortsos, and P. C. Lichtner, On the upscaling of reaction-transport processes in porous media with fast or finite kinetics, *Chem. Eng. Sci*. **57**(13), 2565–2577 (2002).
27. M. Shapiro and H. Brenner, Taylor dispersion of chemically reactive species: Irreversible first-order reactions in bulk and on boundaries, *Chem. Eng. Sci*. **41**(6), 1417–1433 (1986).
28. L. Durlovsky and J. F. Brady, Analysis of the Brinkman equation as a model for flow in porous media, *Phys. Fluids* **30**(11), 3329–3341 (2009).
29. M. Shapiro and M. Brenner, Dispersion of a chemically reactive solute in a spatially periodic model of a porous medium, *Chem. Eng. Sci*. **43**(3), 551–571 (1988).
30. M. Shapiro, R. Fedou, J. Thovert, and P. M. Adler, Coupled transport and dispersion of multicomponent reactive solutes in rectilinear flows, *Chem. Eng. Sci*. **51**(22), 5017–5041 (1996).
31. U. Hornung, *Homogenization and Porous Media*. Springer, New York (1997).
32. P. M. Adler, *Porous Media: Geometry and Transports*. Butterworth-Heinemann, New York (1992).
33. R. C. Acharya, S. E. A. T. M. V. der Zee, and A. Leijnse, Transport modeling of nonlinearly adsorbing solutes in physically heterogeneous pore networks, *Water Resour. Res*. **41**, W02020 (2005).
34. W. G. Gray and C. T. Miller, Thermodynamically constrained averaging theory approach for modeling flow and transport phenomena in porous medium systems: 1. Motivation and overview, *Adv. Water Resour*. **28**(2), 161–180 (2005).
35. Y. Davit, C. G. Bell, H. M. Byrne, L. A. C. Chapman, L. S. Kimpton, G. E. Lang, K. H. L. Leonard et al., Homogenization via formal multiscale asymptotics and volume averaging: How do the two techniques compare? *Adv. Water Resour*. **62**, 178–206 (2013).
36. B. D. Wood, Technical note: Revisiting the geometric theorems for volume averaging, *Adv. Water Resour*. **62**(B), 340–352 (2013).
37. J. H. Cushman, L. S. Bennethum, and B. X. Hu, A primer on upscaling tools for porous media, *Adv. Water Resour*. **25**(8–12), 1043–1067 (2002).
38. H. Arunachalam, S. Onori, and I. Battiato, On veracity of macroscopic Lithium-ion battery models, *J. Electrochem. Soc*. **162**(10), A1940–A1951 (2015).
39. G. de Marsily, *Quantitative Hydrogeology*. Academic Press, San Diego, CA (1986).
40. J. Bear, *Dynamics of Fluids in Porous Media*. Dover Publications, Inc., New York (1972).
41. H. Brenner, Macrotransport Processes, Butterworth-Heinemann Series in Chemical Engineering, Stoneham, MA (1993).

42. J. L. Auriault and P. M. Adler, Taylor dispersion in porous media: Analysis by multiple scale expansions, *Adv. Water Resour.* **4**(18), 217–226 (1995).
43. A. Mikelić, V. Devigne, and C. J. Van Duijn, Rigorous upscaling of the reactive flow through a pore, under dominant Peclet and Damköhler numbers, *SIAM J. Math. Anal.* **38**(4), 1262–1287 (2006).
44. M. A. Peter, Homogenization in domains with evolving microstructure, *C. R. Mécanique* **335**, 357–362 (2007).
45. E. Marušić-Paloka and A. Piatnitski, Homogenization of a nonlinear convection-diffusion equation with rapidly oscillating coefficients and strong convection, *J. Lond. Math. Soc.* **2**(72), 391–409 (2005).
46. S. P. Neuman, Theoretical derivation of Darcy's law, *Acta Mecanica* **25**, 153–170 (1977).
47. H. Darcy, Les fontaines publiques de la ville de dijon, Victor Darmon, Paris, France (1856).
48. J. L. Auriault, C. Geindreau, and C. Boutin, Filtration law in porous media with poor separation of scales, *Transp. Porous Media* **60**, 89–108 (2005).
49. H. C. Brinkman, A calculation of the viscous force exerted by a flowing fluid on a dense swarm of particles, *Appl. Sci. Res.* **A1**, 27–34 (1949).
50. T. Lévy, Fluid flow through an array of fixed particles, *Int. J. Eng. Sci.* **21**, 11–23 (1983).
51. J.-L. Auriault, On the domain of validity of Brinkman's equation, *Transp. Porous Media* **79**, 215–223 (2009).
52. B. Goyeau, T. Benihaddadene, D. Gobin, and M. Quintard, Averaged momentum equation for flow through a nonhomogeneous porous structure, *Transp. Porous Media* **28**, 19–50 (1997).
53. I. Battiato, P. R. Bandaru, and D. M. Tartakovsky, Elastic response of carbon nanotube forests to aerodynamic stresses, *Phys. Rev. Lett.* **105**, 144504 (2010).
54. I. Battiato, Self-similarity in coupled Brinkman/Navier–Stokes flows, *J. Fluid Mech.* **699**, 94–114 (2012).
55. I. Battiato, Effective medium theory for drag-reducing micro-patterned surfaces in turbulent flows, *Eur. Phys. J.* **E37**, 19 (2014).
56. I. Battiato and S. Rubol, Single-parameter model of vegetated aquatic flows, *Water Resour. Res.* **50**(8), 6358–6369 (2014).
57. A. Papke and I. Battiato, A reduced-complexity model for dynamic similarity in obstructed shear flows, *Geophys. Res. Lett.* **40**, 1–5 (2013).
58. G. Blois, J. L. Best, K. T. Christensen, R. J. Hardy, and G. H. S. Smith, Coherent flow structures in the pore spaces of permeable beds underlying a unidirectional turbulent boundary layer: A review and some new experimental results, in J. G. Venditti, J. L. Best, M. Church, and R. J. Hardy (eds.), *Coherent Flow Structures at Earth's Surface*. John Wiley & Sons, Ltd., Chichester, UK (2013).
59. J. R. Philip, Flow in porous media, *Annu. Rev. Fluid Mech.* **2**, 177–204 (1970).
60. S. Whitaker, The forchheimer Equation: A theoretical development, *Transp. Porous Media* **25**, 17–61 (1996).
61. Z. Chen, S. L. Lyons, and G. Qin, Derivation of the forchheimer law via homogenization, *Transp. Porous Media* **44**(2), 325–335 (2001).
62. M. J. S. de Lemos, *Turbulence in Porous Media: Modeling and Applications*. Elsevier Ltd., Oxford, U.K. (2006).
63. J. H. Cushman, D. O. Malley, and M. Park, Anomalous dispersion, renormalization groups, scaling laws and classification: A reflection on recent efforts, *Adv. Water Resour.* **62**(B), 207–214 (2013).
64. W. G. Gray and C. T. Miller, A generalization of averaging theorems for porous medium analysis, *Adv. Water Resour.* **62**(B), 227–237 (2013).
65. Y. Liu and P. K. Kitanidis, A mathematical and computational study of the dispersivity tensor in anisotropic porous media, *Adv. Water Resour.* **62**(B), 303–316 (2013).
66. A. Rabinovich, G. Dagan, and T. Miloh, Effective conductivity of heterogeneous aquifers in unsteady periodic flow, *Adv. Water Resour.* **62**(B), 317–326 (2013).
67. J. A. Ochoa-Tapia, P. Stroeve, and S. Whitaker, Facilitated transport in porous media, *Chem. Eng. Sci.* **46**, 477–496 (1991).
68. B. D. Wood and R. M. Ford, Biological processes in porous media: From the pore scale to the field, *Adv. Water Resour.* **30**(6–7), 1387–1391 (2007).
69. B. D. Wood, K. Radakovich, and F. Golfier, Effective reaction at a fluid-solid interface: Applications to biotransformation in porous media, *Adv. Water Resour.* **30**(6–7), 1630–1647 (2007).
70. T. L. van Noorden and I. S. Pop, A Stefan problem modelling crystal dissolution and precipitation, *IMA J. Appl. Math.* **73**(2), 393–411 (2008).
71. F. Hesse, F. A. Radu, M. Thullner, and S. Attinger, Upscaling of the advection-diffusion-reaction equation with Monod reaction, *Adv. Water Resour.* **32**, 1336–1351 (2009).
72. J. H. Cushman and T. R. Ginn, Nonlocal dispersion in media with continuously evolving scales of heterogeneity, *Transp. Porous Media* **1**, 1–138 (1993).
73. S. P. Neuman, Eulerian–Lagrangian theory of transport in space-time non-stationary velocity fields—Exact nonlocal formalism by conditional moments and weak approximation, *Water Resour. Res.* **29**(3), 633–645 (1993).
74. L. W. Gelhar, C. Welty, and K. R. Rehfeldt, A critical review of data on field-scale dispersion in aquifers, *Water Resour. Res.* **28**(7), 1955–1974 (1992).
75. L. Li, C. Peters, and M. Celia, Upscaling geochemical reaction rates using pore-scale network modeling, *Adv. Water Resour.* **29**, 1351–1370 (2006).
76. M. Dentz, T. L. Borgne, A. Englert, and B. Bijelijc, Mixing, spreading and reaction in heterogeneous media: A brief review, *J. Contam. Hydrol.* **120–121**, 1–17 (2011).
77. A. M. Tartakovsky, D. M. Tartakovsky, and P. Meakin, Stochastic Langevin model for flow and transport in porous media, *Phys. Rev. Lett.* **101**, 044502 (2008).

78. C. Knutson, A. Valocchi, and C. Werth, Comparison of continuum and pore-scale models of nutrient biodegradation under transverse mixing conditions, *Adv. Water Resour.* **30**(6–7), 1421–1431 (2007).
79. A. M. Tartakovsky, P. Meakin, T. D. Scheibe, and R. M. E. West, Simulation of reactive transport and precipitation with smoothed particle hydrodynamics, *J. Comput. Phys.* **222**, 654–672 (2007).
80. A. M. Tartakovsky, G. Redden, P. C. Lichtner, T. D. Scheibe, and P. Meakin, Mixing-induced precipitation: Experimental study and multi-scale numerical analysis, *Water Resour. Res.* **44**, W06S04 (2008).
81. B. Zinn, L. C. Meigs, C. F. Harvey, R. Haggerty, W. J. Peplinski, and C. F. von Schwerin, Experimental visualization of solute transfer processes in two-dimensional conductivity fields with connected regions of high conductivity, *Environ. Sci. Technol.* **38**, 3916–3926 (2004).
82. I. Battiato, D. M. Tartakovsky, A. M. Tartakovsky, and T. Scheibe, On breakdown of macroscopic models of mixing-controlled heterogeneous reactions in porous media, *Adv. Water Resour.* **32**, 1664–1673 (2009).
83. I. Battiato and D. M. Tartakovsky, Applicability regimes for macroscopic models of reactive transport in porous media, *J. Contam. Hydrol.* **120–121**, 18–26 (2011).
84. F. Boso and I. Battiato, Homogenizability conditions of multicomponent reactive transport processes, *Adv. Water Resour.* **62**, 254–265 (2013).
85. S. Molins, D. Trebotich, C. I. Steefel, and C. P. Shen, An investigation of the effect of pore scale flow on average geochemical reaction rates using direct numerical simulation, *Water Resour. Res.* **48**, W03527 (2012).
86. T. D. Scheibe, W. A. Perkins, M. C. Richmond, M. I. McKinley, P. D. J. Romero-Gomez, M. Oostrom, T. W. Wietsma, J. A. Serkowski, and J. M. Zachara, Pore-scale and multiscale numerical simulation of flow and transport in a laboratory-scale column, *Water Resour. Res.* **51**(2), 1023–1035 (2015).
87. M. L. Brusseau and P. S. C. Rao, Non-equilibrium and dispersion during transport of contaminants in groundwater: Field-scale process, in H. Kobus and W. Kinzelbach (eds.), *Contaminant Transport in Groundwater*. A. A. Balkema, Brookfield, VT, pp. 237–244 (1989).
88. H. Gaber, W. Inskeep, S. Comfort, and J. Wraith, Non-equilibrium transport of atrazine through large intact soils cores, *Soil Sci. Soc. Am. J.* **59**, 60–67 (1995).
89. E. Weinan, B. Engquist, and Z. Huang, Heterogeneous multiscale method: A general methodology for multiscale modeling. *Phys. Rev. B* **67**(9), 092101 (2003).
90. T. Scheibe, E. Murphy, X. Chen, A. Rice, K. Carroll, B. Palmer, A. Tartakovsky, I. Battiato, and B. Wood, An analysis platform for multiscale hydrogeologic modeling with emphasis on hybrid multiscale methods, *Ground Water* **53**(1), 38–56 (2015).
91. E. Weinan, *Principles of Multiscale Modeling*. Cambridge University Press, New York (2011).
92. J. C. Parker and A. J. Valocchi, Constraints on the validity of equilibrium and first-order kinetic transport models in structured soils, *Water Resour. Res.* **22**, 399–407 (1986).
93. J. Griffioen, Suitability of the first-order mass transfer concept for describing cyclic diffusive mass transfer in stagnant zones, *J. Contam. Hydrol.* **34**, 155–165 (1998).
94. F. Cherblanc, A. Ahmadi, and M. Quintard, Two-medium description of dispersion in heterogeneous porous media: Calculation of macroscopic properties, *Water Resour. Res.* **39**, 1154 (2003).
95. P. Leemput, C. Vandekerckhove, W. Vanroose, and D. Roose, Accuracy of hybrid lattice Boltzmann/finite difference schemes for reaction diffusion systems. *Multiscale Model. Simul.* **6**(3), 838–857 (2007).
96. A. M. Tartakovsky, D. M. Tartakovsky, T. D. Scheibe, and P. Meakin, Hybrid simulations of reaction-diffusion systems in porous media, *SIAM J. Sci. Comput.* **30**(6), 2799–2816 (2008).
97. P. Langlo and M. S. Espedal, Macrodispersion for two-phase, immiscible flow in porous media, *Adv. Water Resour.* **17**, 297–316 (1994).
98. Y. Efendief, L. J. Durlofsky, and S. H. Lee, Modeling of subgrid effects in coarse-scale simulations of transport in heterogeneous porous media, *Water Resour. Res.* **36**(8), 2031–2041 (2000).
99. Y. Efendief and L. J. Durlofsky, Numerical modeling of subgrid heterogeneity in two phase flow simulations, *Water Resour. Res.* **38**(8), 1128–1138 (2002).
100. Y. Efendief and L. J. Durlofsky, A generalized convection-diffusion model for subgrid transport in porous media, *Multiscale Model. Simul.* **1**(3), 504–526 (2003).
101. E. Villa, A. Balaeff, L. Mahadevan, and K. Schulten, Multiscale method for simulating protein-DNA complexes, *Multiscale Model. Simul.* **2**, 527–553 (2004).
102. X. Yue and E. Weinan, Numerical methods for multiscale transport equations and application to two-phase porous media flow, *J. Comput. Phys.* **210**, 656–675 (2005).
103. D. G. Vlachos, A. B. Mhadeshwar, and N. S. Kaisare, Hierarchical multi-scale model-based design of experiments, catalysts, and reactors for fuel processing, *Comp. Chem. Eng.* **30**, 1712–1724 (2006).
104. M. Christie, Upscaling for reservoir simulation, *J. Petrol. Technol.* **48**, 1004–1010 (1996).
105. B. Berkowitz, H. S. Berkowitz, and H. Scher, Theory of anomalous chemical transport in random fracture networks, *Phys. Rev. E* **57**(5), 8585–8569 (1998).
106. D. A. Benson, S. W. Wheatcraft, and M. M. Meerschaert, Application of a fractional advection-dispersion equation, *Water Resour. Res.* **36**(6), 1403–1412 (2000).
107. J. Carrera, X. Sánchez-Vila, I. Benet, A. A. Medina, G. Galarza, and J. Guimerà, On matrix diffusion: Formulations, solution methods and qualitative effects, *Hydrogeol. J.* **6**, 178–190 (1998).

108. F. J. Alexander, A. L. Garcia, and D. M. Tartakovsky, Algorithm refinement for stochastic partial differential equations: 1. Linear diffusion, *J. Comput. Phys.* **182**, 47–66 (2002).
109. F. J. Alexander, A. L. Garcia, and D. M. Tartakovsky, Algorithm refinement for stochastic partial differential equations: II. Correlated systems, *J. Comput. Phys.* **207**(2), 769–787 (2005).
110. F. J. Alexander, A. L. Garcia, and D. M. Tartakovsky, Noise in algorithm refinement methods, *Comput. Sci. Eng.* **7**(3), 32–38 (2005).
111. A. Malevanets and R. Kapral, Solute molecular dynamics in a mesoscale solvent, *J. Chem. Phys.* **112**, 7260–7269 (2000).
112. P. V. Coveney and P. W. Fowler, Modelling biological complexity: A physical scientist's perspective, *J. R. Soc. Interface* **2**, 267–280 (2005).
113. I. Battiato, D. M. Tartakovsky, A. M. Tartakovsky, and T. D. Scheibe, Hybrid models of reactive transport in porous and fractured media, *Adv. Water Resour.* **34**(9), 1140–1150 (2011).
114. M. Youzefzadeh and I. Battiato, Nonintrusive hybrid models of reactive transport in fractured media: An immersed boundary method approach, *Water Resour. Res.* submitted (2016).
115. M. Yousefzadeh and I. Battiato, Second-order IBM reconstruction scheme through normal boundary interpolation, *J. Comput. Phys.* submitted (2016).
116. M. Peszynska, Q. Lu, and M. Wheeler, Coupling different numerical coupling different numerical algorithms for two phase fluid flow, in J. Whiteman (ed.), *Mathematics of Finite Elements and Applications X*. Elsevier, Oxford, UK, pp. 205–214 (2000).
117. M. Peszynska, Q. Lu, and M. Wheeler, Multiphysics coupling of codes, in L. Bentley, J. Sykes, C. Brebbia, W. Gray, and G. Pinder (eds.), *Computational Methods in Water Resources*. A.A. Balkema, pp. 175–182 (2000).
118. M. Peszynska, M. Wheeler, and I. Yotov, Mortar upscaling for multiphase flow in porous media, *Computat. Geosci.* **6**(1), 73–100 (2002).
119. M. T. Balhoff, S. G. Thomas, and M. F. Wheeler, Mortar coupling and upscaling of pore-scale models, *Computat. Geosci.* **12**(1), 15–27 (2008).
120. T. Y. Sun, Y. Mehmani, and M. T. Balhoff, Hybrid multiscale modeling through direct numerical substitution of pore-scale models into near-well reservoir simulators, *Energ. Fuels* **26**, 5828–5836 (2012).
121. T. Y. Sun, Y. Mehmani, and M. T. Balhoff, Pore to continuum upscaling of permeability in heterogeneous porous media using mortars, *Int. J. Oil Int. J. Gas Coal Technol.* **5**(2–3), 249–266 (2012).
122. Y. Mehmani, T. Sun, M. T. Balhoff, P. Eichhubl, and S. Bryant, Multiblock pore-scale modeling and upscaling of reactive transport: Application to carbon sequestration, *Transp. Porous Media* **95**(2), 305–326 (2012).
123. Y. Mehmani, M. Oostrom, and M. T. Balhoff, A streamline splitting pore-network approach for computationally inexpensive and accurate simulation of species transport in porous media, *Water Resour. Res.* **50**(3), 2488–2517 (2014).
124. Y. Tang, A. J. Valocchi, and C. J. Werth, A hybrid pore-scale and continuum-scale model for solute diffusion, reaction, and biofilm development in porous media, *Water Resour. Res.* **51**(3), 1846–1859 (2015).
125. M. Prat, On the boundary conditions at the macroscopic level, *Transp. Porous Media* **4**, 259–280 (1989).
126. S. B. Pope, *Turbulent Flows*. Cambridge University Press, New York (2000).
127. Y. He and J. F. Sykes, On the spatial-temporal averaging method for modeling transport in porous media, *Transp. Porous Media* **22**, 1–51 (1996).
128. P. Wang, P. Quinland and D. M. Tartakovsky, Effects of spatio-temporal variability of precipitation on contaminant migration in the vadose effects of spatio-temporal variability of precipitation on contaminant migration in the vadose zone, *Geophys. Res. Lett.* **36**, L12404 (2009).
129. S. Taverniers, F. J. Alexander, and D. M. Tartakovsky, Noise propagation in hybrid models of nonlinear systems: The ginzburg-landau equation, *J. Comput. Phys.* **262**, 313–324 (2014).